

Aeroacoustic investigation of airfoil at near stall conditionsPrateek Jaiswal,^{a)} Jose Rendón,^{b)} and Stéphane Moreau^{b)}

(Dated: 6 July 2023)

This paper presents a detailed aeroacoustic investigation of a Controlled-Diffusion airfoil at near stall condition. The study aims at answering two research questions: identify the flow mechanism responsible for separation noise for an airfoil near stall conditions and whether the noise is generated by a dipole for airfoil close to stall and can be quantified by Amiet's diffraction theory. The study uses synchronized PIV, RMP and far-field microphone measurements to perform experiments at two chord based Reynolds numbers of about 150,000 and 250,000. The results show that when the airfoil is placed at a higher angle of attack, such as 15° , strong amplification of flow disturbance is seen, resulting in the rolling up of the shear layer in the aft-region of the airfoil, forming large coherent structures. While these rollers play a central role in the increase in noise due to flow separation, the flapping of shear layer does not contribute to the separation noise. The present study conclusively shows that separation noise is dipolar in nature, and that the quadrupolar contribution for low-speed airfoils at near-stall conditions can be neglected. However, the increase in flow disturbances measured close to the trailing-edge of the airfoil implies that the assumption of small amplitude disturbance is no longer valid, which is the central premise of the thin linearized airfoil theory. Outside the frequency range at which flow separation operates, Amiet's theory is able to predict the far-field noise even at high angles of attack.

^{a)}Electronic mail: jaiswalprateek@protonmail.com; Department of Mechanical Engineering, University of Sherbrooke, Sherbrooke, QC, CA.

^{b)}Department of Mechanical Engineering, University of Sherbrooke, Sherbrooke, QC, CA.

NOMENCLATURE

C	Airfoil chord
c_0	Speed of sound
C_p	Mean pressure coefficient
C_{prms}	Root-mean-square of the wall-pressure coefficient
$\overline{E_{11}}$	Pre-multiplied turbulent energy spectra
H	Boundary layer shape factor
M_∞	Inlet Mach number
p_∞	Inlet static pressure
p_{rms}	root-mean-square of the wall pressure
p'_a	Far-field acoustic pressure
p'_w	Fluctuating wall-pressure
R_{ij}	Second order two-point zero time delay correlation
Re_c	Reynolds number based on the chord
S_{pp}	Far-field acoustic power spectral density
u_i	Fluctuating velocity component
U_c	Convective speed of wall-pressure fluctuations
U_∞	Inlet velocity
U_e	Boundary layer edge velocity
U_1, U_2, U_3	Mean velocity in trailing edge reference frame
$\overline{u_1 u_1}, \overline{u_2 u_2}, \overline{-u_1 u_2}$	Root-mean-square of velocity fluctuations in trailing edge reference frame
$-\rho \overline{u_1 u_2}_{max}$	maximum Reynolds shear stress
V_x, V_y	Mean velocity in wind tunnel reference frame
x, y, z	Wind tunnel coordinate system
x_1, x_2, x_3	Coordinate system aligned with the airfoil trailing edge
x'_1, x'_2, x'_3	Coordinate system aligned with the airfoil leading edge
δ_{95}	Boundary layer thickness based on 95% of U_e
δ^*	Boundary layer displacement thickness
Λ	Dimensionless radiation ratio

θ	Boundary layer momentum thickness
ρ	Constant air density

I. INTRODUCTION

Airfoil trailing-edge noise is dominant in a host of engineering applications. Several of the distinct mechanisms, which are referred as airfoil self-noise, are related to scattering of pressure gust past the airfoil trailing edge. Among them, noise due to flow separation is found to be dominant at high angles of attack, where large scale flow separation may occur. This is particularly the case for some wind turbine architectures, such as the H-Darrieus type wind turbine [Venkatraman *et al.* 2023]. Therefore, accurate models are needed during the pre-design phase to estimate acoustic noise by such machines. To achieve this a better understanding of the noise generation mechanism is needed. Nevertheless, only few comprehensive aeroacoustic studies have been performed, for airfoils placed at high angles of attack [Kalyani, Moreau, and Ragni 2022; Lacagnina *et al.* 2019; Moreau and Roger 2009; Raus *et al.* 2022; Zang, Mayer, and Azarpeyvand 2021]. As such, the overall objectives of the present manuscript are to identify the dominant flow mechanism(s) responsible for separation noise, and test the applicability of diffraction theory [Amiet 1976] to predict noise at high angles of attack.

Numerically, Moreau and co-workers had performed several high-fidelity incompressible simulations for airfoil at high incidence almost a decade ago [Christophe and Moreau 2008; Moreau, Christophe, and Roger 2008; Moreau, Roger, and Christophe 2009]. In these simulations, an isolated airfoil installed in an open-jet anechoic wind tunnel (the test configuration) was simulated as opposed to the full scale wind turbine [Venkatraman *et al.* 2023]. As such only the noise due to the boundary-layer and its separation were studied. The far-field noise was quantified using both acoustic analogies [Curle 1955; Ffowcs Williams and Hall 1970] and Amiet’s (1976) diffraction theory. Christophe and Moreau [2008] reported over-prediction of the wall-pressure by the LES, and the far-field acoustic spectra estimated by Amiet’s (1976) model to be 10 dB higher than the measurements. In particular, this disagreement was present only at the low frequency, where the noise due to separation is expected to be the dominant mechanism. Similarly, the semi-empirical models for far-field noise based on

Amiet’s (1976) theory, referred to as MODA [Bertagnolio *et al.* 2017], have been shown to yield poor results. However, the reason for this disagreement when predicting separation noise with Amiet’s (1976) model is unknown and requires further investigation.

More recently, compressible simulations have been performed by Turner and Kim [2022] to quantify the individual contributions of equivalent source type (dipole and quadrupole) from low-speed airfoils in near stall conditions. They achieve this by subtracting noise estimated by the solid formulation of Ffowcs Williams and Hawkings’s (1969) acoustic analogy from the noise estimated by the permeable formulation. Turner and Kim [2022] show that the noise contribution by quadrupole sources is significant, when an airfoil is placed at high incidence. However, while the porous formulation is complete, the solid formulation ignores the correlation between the dipole and quadrupole noise sources. This can lead to spurious directivity patterns as already demonstrated by Spalart *et al.* [2019]. Nevertheless, it is important to quantify the individual contributions of various equivalent source types that may contribute to far-field noise.

While equivalent noise sources are an important metric in aeroacoustics research, they are by no means unique. This is because the multipole expansion [Goldstein 1976] dictates that one equivalent image source can be replaced by another. For instance, a quadrupole can be expressed as two dipoles that are of equal strength but in phase opposition. As such correct identification of equivalent noise source cannot by itself describe or confirm the precise flow mechanism behind separation noise. As such it is imperative to perform a detailed flow quantification and analysis to understand the noise mechanism. Previously, Brooks, Pope, and Marcolini [1989] hypothesized that airfoil separation noise results from the interaction between turbulent structures in the shear layer and the airfoil trailing-edge, as separated structures are convected past the airfoil, resulting in significant pressure fluctuations. However, previous experiments were unable to accurately identify the noise mechanism, as flow-field measurements were unavailable.

More recently, using PIV and synchronized wall-pressure and hot-wire measurements, Lacagnina *et al.* [2019] identified three possible distinct noise generation mechanisms to explain noise generation by an airfoil close to stall. Importantly, all of these mechanisms were linked to instabilities in the shear layer and were localized in a region within the separated shear layer away from the wall. The separated shear layer may not only result in a substantial increase in the contribution of quadrupole noise [Turner and Kim 2022],

but may also invalidate the unsteady Kutta condition. This is because the latter relies on the flow leaving the airfoil trailing edge smoothly. Furthermore, separation noise is dominant for airfoil placed at high angles of attack. Therefore, the central premise of the thin-airfoil linearized theory may not hold for such cases because the amplitude of the induced disturbance by the flow separation may not be small. Evidently, changes may occur in resulting radiation ratio, and thus Amiet’s (1976) radiation factor may not be able to correctly quantify the hydrodynamic-to-acoustic conversion [see figures 3 and 12 of Roger and Moreau 2004, for instance]. Therefore, in the present manuscript, we ask the question: can the separation noise be fully quantified using a dipole source, such as those outlined in Amiet’s diffraction theory? If so, are there other possible mechanisms of noise generation that may explain noise generation due to an airfoil close to stall? Furthermore, is the mechanism behind the separation noise universal ?

To this end, aeroacoustic measurements have been performed in the anechoic flow facility at Université de Sherbrooke. In particular, planar PIV measurement, wall-pressure and far-field acoustic measurements have been achieved. For the present study, a Controlled-Diffusion (CD) airfoil is used. These measurements have been performed at a fixed geometric angle of attack of 15° . For the CD airfoil at this angle of attack, flow separation near the leading-edge region was reported by Christophe and Moreau [2008]. As such, the present aeroacoustic investigation is performed to understand noise due to flow separation, for an airfoil that is close to stall conditions [Kalyani, Moreau, and Ragni 2022]. Comparing the flow and pressure characteristics between the present case and that reported earlier, where the boundary-layer is fully attached near the trailing-edge of the airfoil [see Jaiswal *et al.* 2020; Wu, Moreau, and Sandberg 2019; 2020, for instance], is expected to elucidate the true contribution of separation noise.

II. EXPERIMENTAL SET-UP AND INSTRUMENTATION:

The aero-acoustic measurements were performed in the anechoic wind tunnel at Université de Sherbrooke (UdeS). The anechoic room, is about $7 \times 5.5 \times 4 \text{ m}^3$ in dimension. The open jet has a dimension of $50 \times 30 \text{ cm}^2$, and can achieve a maximum velocity of 40 m/s. As the temperature of the open jet can be controlled, all the measurements are performed at a constant free-stream density ρ .

The CD airfoil is placed at a 15° geometric angle of attack with the help of plexiglass plates of thickness 4.25 mm laser cut to reduce uncertainty in angle of attack while placing the airfoil and at the same time giving good optical access. All the measurements are performed at a free-stream velocity U_∞ of 16 m/s and 28 m/s, which respectively corresponds to Mach numbers $M_\infty \equiv U_\infty/c_0 \simeq 0.05$ and $M_\infty \simeq 0.08$ (c_0 speed of sound) and Reynolds numbers based on the airfoil chord length C and the free-stream velocity of $Re_c \simeq 1.5 \times 10^5$ and $Re_c \simeq 2.5 \times 10^5$.

A. Planar PIV measurements setup

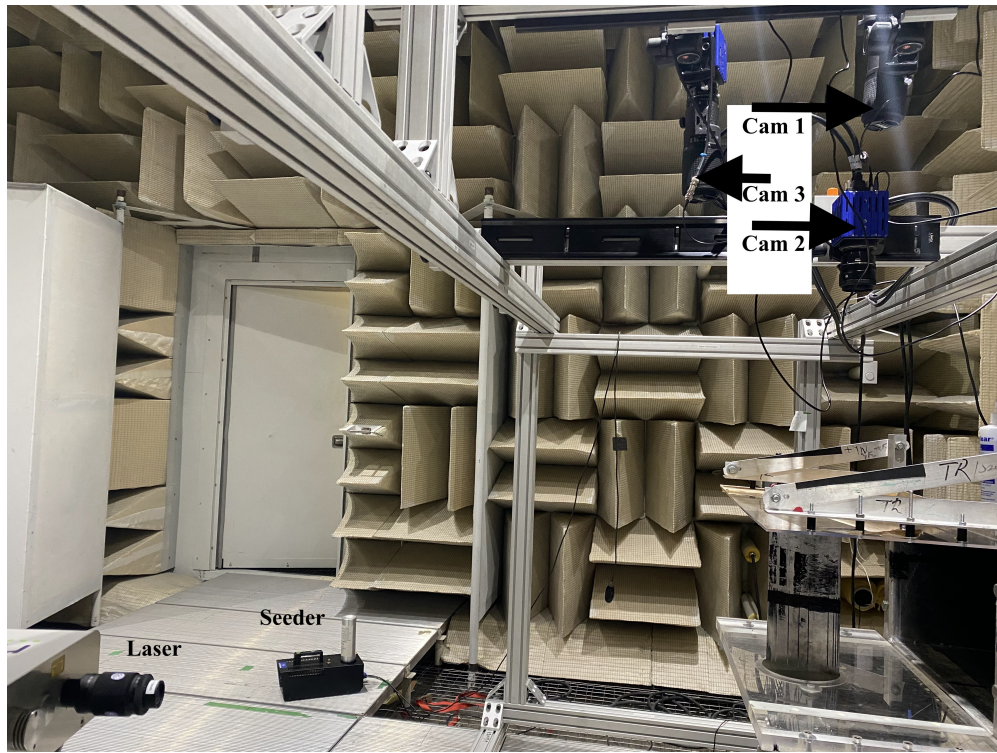


FIG. 1. Planar-PIV setup

Two-dimensional PIV measurements were performed on the suction side of the airfoil, as shown in figure 1. Three sCMOS cameras, with a 5.5 megapixel sensors each, were used to acquire images in a dual frame mode. A ND:YAG dual pulsed laser from Lavision was used for illumination. The light sheet for Planar PIV was generated with a set of spherical lenses and a diverging cylindrical lens with a focal length of -20 mm. Tracer particles of about $1 \mu\text{m}$ were generated to seed the flow. The images were recorded for each case at

TABLE II. Parameters used for the Planar PIV boundary-layer measurements.

Parameters	Leading-edge (M1)	Mid-chord (M2)	Trailing-edge (M3)
Number of Images	1800	1400	1800
Interrogation window [pixel ²]	4×4	4×4	4×4
Lenses focal Length [mm]	200	50	200
Final window size [mm ²]	0.11×0.11	0.32×0.32	0.09×0.09
Maximum particle image displacement [pixel]	20	24	20

an acquisition frequency of 2 Hz. Inter-frame time was increased until the cross-correlation coefficient remains between 0.6 – 0.9. The resulting inter-frame time meant particle image displacement of more than 20 pixels was achieved in the free stream. This ensures low relative error ($\sim 0.5\%$) in the estimation of particle image displacement. The data collected at a free-stream velocity of $U_\infty = 16$ m/s were processed using Lavision’s Davis 8 software while for the $U_\infty = 28$ m/s case they were processed with the newer Davis 10 software. The final vector calculations were performed on the computer clusters from Digital Research Alliance of Canada. For $U_\infty = 16$ m/s case, a total of 11 passes were used for the multi-grid scheme, starting with an initial window of 128×128 pixels to the final window size of 4×4 pixels. In the iterative multi-grid scheme, an overlap of 75 % and an elliptical weighting (elongated in the mean-flow direction) is used. The final window size was about 0.0923×0.0923 mm². In contrast, for the $U_\infty = 28$ m/s case, a reduced window overlap of 50 % was used while keeping all the other parameters the same as for the $U_\infty = 16$ m/s case. This was done to accelerate the vector calculations and to reduce the size of the final vector field.

B. Steady wall-pressure measurements

Figure 2 shows the pinholes located along the chord of the airfoil, which are used to measure the mean wall-pressure coefficient. There are in total 21 probes on both suction and pressure sides of the airfoil, 18 of them are placed in the streamwise direction and the last 3 in the spanwise direction. Pinholes on the pressure side of the airfoil are labelled as 4,

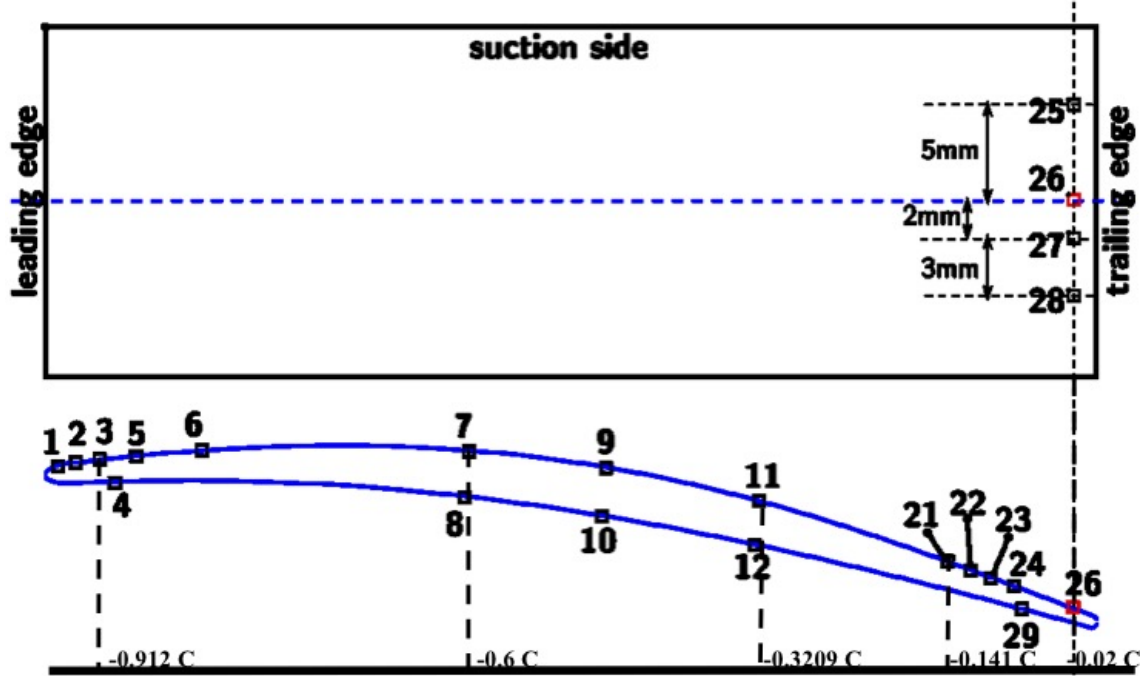


FIG. 2. Location of pinholes on the CD airfoil. Some of the pinhole locations on the suction side of the airfoil have been indicated.

8, 10, 12 and 29, whereas those on the suction side are 1 to 6 at the leading edge, 7, 9 and 11 at mid-chord and 21 to 28 at the trailing edge (see figure 2). The differential pressure is measured using an array of miniature amplified low pressure sensors in order to get a full reading along the airfoil chord [Neal 2010]. These miniature amplified low pressure sensors have an accuracy of 0.25% Full Scale (FSS), which is between 1244.2 – 248.84 Pa. Details on the setup and acquisition can be found in Jaiswal [2020]. In the current paper, the wall differential pressure are normalized by inlet free stream dynamic pressure, which yields the mean pressure coefficient $C_p \equiv (p - p_\infty)/(0.5 \rho U_\infty^2)$ with p_∞ the inlet pressure.

C. Unsteady wall-pressure measurements

The pinholes on both sides of the airfoil are also connected to Remote Microphone Probes (RMP) to record unsteady static wall-pressure measurements [Moreau and Roger 2005; Perennes and Roger 1998]. For the present set of experiments, Knowles FG 23329-P07 miniature microphones were used. These microphones have a flat response over a large range of frequency (0.1 – 10 kHz), and have a nominal sensitivity of 22.4 mV/Pa. The pinhole

diameter of 0.5 mm ensures spectral averaging is avoided well beyond 10 kHz [Grasso *et al.* 2019]. As these microphones are connected remotely to the pinhole, a correction in phase and magnitude is needed. This is achieved following the methodology outlined by Jaiswal *et al.* [2020].

D. Hot wire measurements

Hot wire anemometry (HWA) is used to investigate the spectral content of the velocity disturbance over the airfoil. The HWA probe is placed directly above RMP 26 ($x/C = 0.98$), on the suction side of airfoil. The hot wire measurements were performed using a TSI 1210 – T 1.5 single wire probe. The probe consists of a platinum coated tungsten wire with a 0.0038 mm diameter and a 1.27 mm length, which satisfies the recommended wire length-to-diameter ratio of 200 [Ligrani and Bradshaw 1987]. The hot wire probe was connected to a TSI IFA 300 anemometer operating in Constant Temperature Anemometry (CTA) mode. The output signals of this anemometer were recorded with 25600 kHz acquisition frequency using a NI 9234 24 bit module. In order to attenuate any unwanted parasitic noise, a low pass filter of 1000 Hz was applied. Based on previous wall-pressure measurements [Moreau and Roger 2005] no substantial contributions of velocity disturbances beyond this frequency is expected for the 15° angle-of-attack case. Furthermore, the HWA were performed only at $U_\infty = 16$ m/s. The total recording time for each of these point-wise measurements was about 60 seconds. For more details on the setup the reader is referred to Jaiswal [2020].

E. Acoustic measurements

Far-field acoustic pressure was measured using Integrated Circuit Piezoelectric (ICP) microphones with a 1/2 inch diaphragm. The microphones are placed in the airfoil mid-chord plane. In total 8 microphones were placed on an circular arc around the airfoil at a distance of 1.21 m (or about 10 times the chord length) to ensure they are in an acoustic far-field location. The microphones were calibrated using a B&K piston-phone, which ensures the calibration uncertainty is within 0.2 dB.

F. Synchronized measurements

In order to relate the near-field velocity disturbance field to the resultant far-field acoustic noise, synchronized velocity-pressure measurements have been performed as previously done at a lower 5° angle-of-attack [Jaiswal *et al.* 2022]. Furthermore, the wall-pressure measurements were also synchronized to study the footprint of velocity disturbances on the wall. To obtain acoustic directivity pattern caused by diffraction of unsteady gust, the far-field microphones were synchronized with the RMPs. The near-field and far-field pressure measurements are time resolved compared to PIV measurements, which has a limited time resolution. As such, the acquisition frequency for all the measurements performed are set to powers of two. In particular, the PIV measurements were performed at 2 Hz while unsteady near and far-field pressure were recorded at an acquisition frequency of 65536 Hz (or 2^{16} Hz). The synchronization between PIV and pressure measurements is achieved using the procedure outlined by Henning *et al.* [2008], where further details on the implementation can be found.

III. RESULTS

To ensure that the flow facility and installation do not dictate overall flow dynamics [see Moreau and Roger 2005; Wu *et al.* 2016, for instance], the mean wall-pressure coefficient has first been compared. The results in two different facilities, in which the CD airfoil has been tested in within a 50 cm wide jet, show an overall good agreement over most of the airfoil chord, C , as shown in figure 3. (x, y) represents the fixed laboratory reference frame at the airfoil midspan, x being parallel to the jet axis and oriented with the flow. The origin of the reference frame is taken at the airfoil trailing edge. Repeatability tests at UdeS have also been achieved [Kalyani, Moreau, and Ragni 2022].

Previous experimental and numerical studies on this airfoil [Christophe, Anthoine, and Moreau 2008; Kalyani, Moreau, and Ragni 2022; Moreau and Roger 2005] have reported an increase in low-frequency noise, when it is placed at a high angle of attack. This observation is confirmed by the far-field microphone measurements shown in figure 4, which shows an overall increase in low frequency sound pressure levels when comparing the 8° and 15° cases for the two Reynolds numbers. As shown in figure 4, this is also consistent with the previous

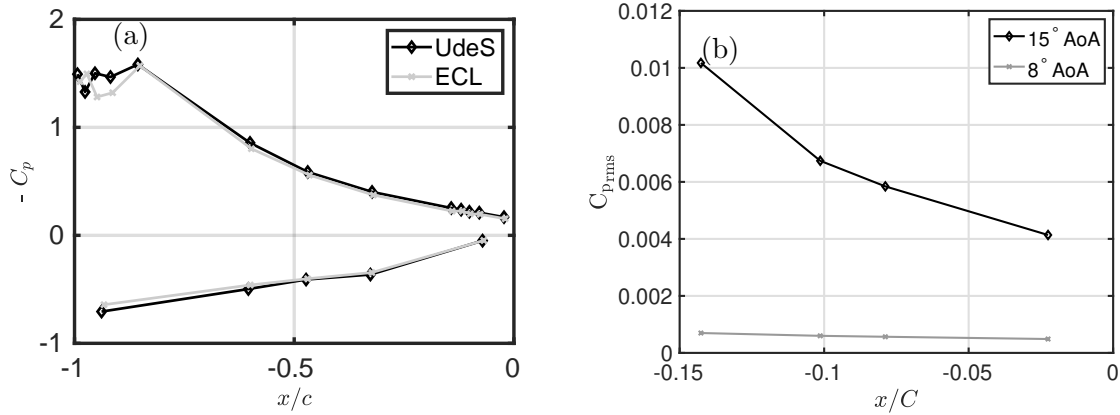


FIG. 3. (a) Mean wall-pressure coefficient ($-C_p$) in two different anechoic wind tunnels; (b) r.m.s of wall-pressure coefficient ($C_{p,rms}$) for RMPs 21, 23, 24 and 26 at $U_\infty = 16$ m/s.

measurements by Moreau and Roger [2005] (open symbols). This noise increase is most likely linked to an overall increase in r.m.s levels of wall pressure close to the trailing-edge region, as shown in figure 3 (b). As the overall goal of the present manuscript is to identify flow mechanisms responsible for separation noise and to test the applicability of diffraction theory [Amiet 1976], the cause (flow disturbances) to the effect (far-field noise) will be established with the help of the latter.

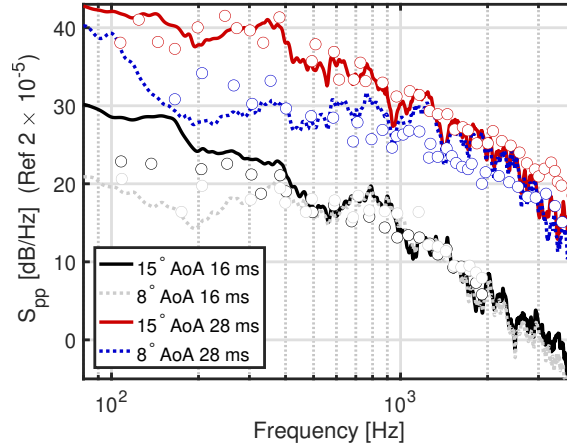


FIG. 4. Sound pressure level at 1.2 m from the airfoil trailing edge on the suction side. Open circles for ECL measurements [Moreau and Roger 2005]

Amiet's model and its extension [Amiet 1976; Moreau and Roger 2009; Roger and Moreau 2005; 2012] relies on Curle's analogy combined with a compressible linearized Euler model for the wall-pressure fluctuations on an infinitely thin flat plate seen as equivalent dipoles.

The PSD of the far-field acoustic pressure at any observer located at $\mathbf{X} = (X_1, X_2, X_3)$, for any angular frequency ω , generated by a flat plate of chord length C and span L then reads:

$$S_{pp}(\mathbf{X}, \omega) \approx \left(\frac{k C X_2}{4\pi S_0^2} \right)^2 \frac{L}{2} \left| \mathcal{I} \left(\frac{\omega}{U_c}, k \frac{X_3}{S_0} \right) \right| \Phi_{pp}(\omega) l_z \left(\omega, k \frac{X_3}{S_0} \right), \quad (1)$$

where k is the acoustic wave number, S_0 the corrected distance to the observer, \mathcal{I} the analytical radiation integral (or acoustic transfer function) given in Roger and Moreau [2005], U_c the streamwise convection velocity, Φ_{pp} the wall-pressure spectrum and l_z the spanwise coherence length.

In summary, the wall-pressure field can be characterized by the PSD of wall-pressure fluctuations, the convection velocity and the spanwise correlation length. In order to explain the increase in the low frequency far-field acoustic spectra, the statistical description of the incident wall-pressure field will be explored in the next section.

A. Unsteady wall-pressure field

Figure 5 shows PSD measurements using RMPs on the suction side of the airfoil along its chord. The first two probes located at the leading edge, show rapid decay in spectral energy most likely because of the laminar nature of the boundary layer. The humps and peaks observed in RMP 3 probe ($x/C \simeq 0.09$) can be linked to boundary-layer instabilities [Jaiswal *et al.* 2020], which are present due to the existence of a Laminar Separation Bubble (LSB). RMP 5 ($x/C \simeq 0.15$) onward the wall-pressure spectra decay is much slower than it was for the first three probes, suggesting a possible turbulent re-attachment. Near the mid-chord region (RMP 9), the wall-pressure statistics almost attains a -5 slope at high-frequencies, suggesting a mean attached turbulent boundary layer.

On the aft part of the airfoil, an almost constant gradient in the wall-pressure spectra, of $f^{-2.2}$, emerges in the mid-frequency range. Similar observations were made by Zang, Mayer, and Azarpeyvand [2021] who used the NACA-65-410 airfoil for their study at high angles of attack, and by Raus *et al.* [2022] on the oscillatory NACA-0012 airfoil in the similar light-stall flow regime. In contrast, at low frequencies, the wall-pressure spectrum becomes flat to an extent that its slope is near zero for probes beyond RMP 9. As such, the classical f^2 [Goody 2004] scaling at low frequency is not observed. It is hypothesized that this change in slope is more linked to the presence of the jet, which predominantly contributes to the low

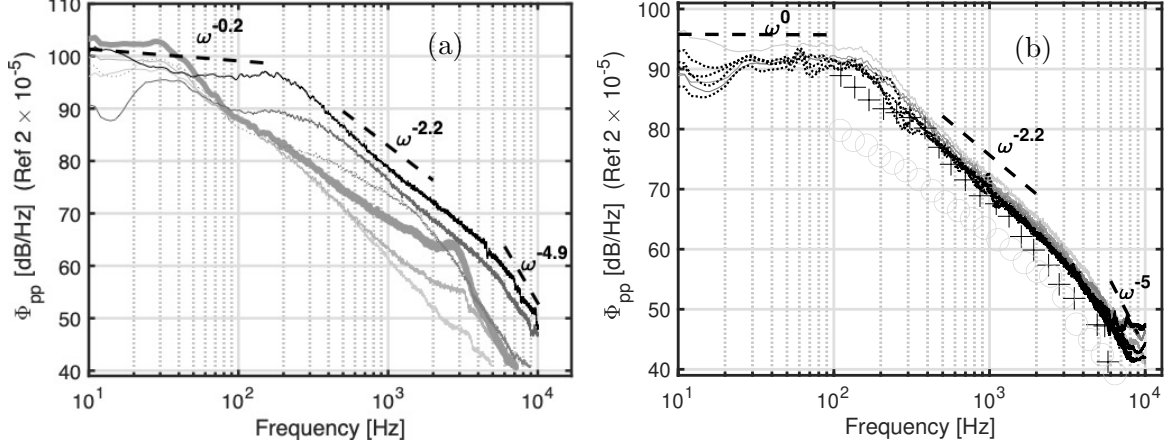


FIG. 5. PSD of wall-pressure fluctuations at $Re_c = 150000$ on the airfoil suction side (color transition from gray to black with increase in x/C): (a) RMP 1 to 9 (thick solid line to highlight RMP 3); (b) RMP 21-28 (black dotted lines for spanwise sensors. Black plus for LES [Christophe and Moreau 2008], and grey circles for ECL measurements [Moreau and Roger 2005]).

frequency and interacts more with the airfoil at high angle of attacks. At higher frequencies, a constant spectral slope of f^{-5} emerges, which is consistent with previous studies made on the CD airfoil [Jaiswal 2020]. Overall, the spectra become statistically similar beyond $0.85 c$. To quantify the effects of mean pressure gradient on wall-pressure fluctuations, differences in PSD between the airfoil at 8° and 15° angles of attack at $Re_c \simeq 150000$ are plotted in figure 6 for the trailing-edge sensors 21 – 25 only between 10 and 1000 Hz. An increase in spectral content is clearly shown for the 15° case compared to the 8° case [Jaiswal 2020].

The second quantity of interest, the convection velocity U_c , was estimated by correlation analysis between two RMPs, 23 and 24, which are separated by a finite streamwise distance (about $0.02 C$). This was performed at several band-passed frequencies to obtain the convection velocity at frequencies where the separation noise dominates. The results obtained are shown in figure 7. Open circles represent the 15° angle-of-attack case, while cross symbols stand for the 8° angle-of-attack case. The dashed line refers to the mean convection velocity ($0.75 U_\infty$) estimated by Moreau and Roger [2005] from the phase slope of two sensors at the trailing edge at 15° and 16 m/s. The present results are therefore consistent with the previous ECL measurements and also with the estimate provided by Grasso *et al.* [2019] based on the direct numerical simulation [Wu, Moreau, and Sandberg 2020] for the 8° case ($0.72 U_\infty$). The lower value at 400 Hz is also consistent with that reported

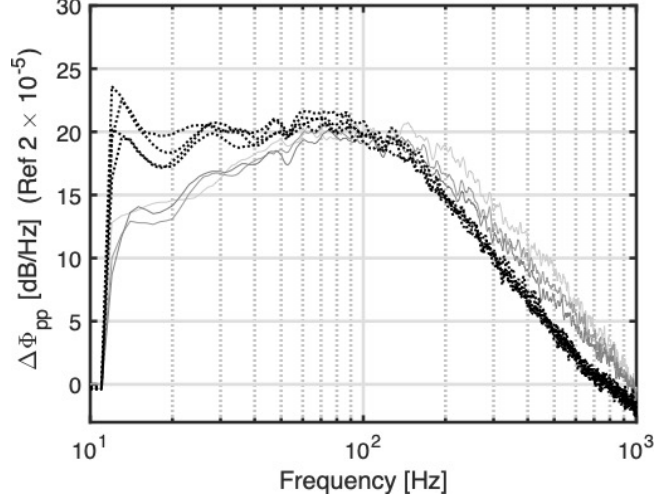


FIG. 6. PSD differences between the 15° and 8° cases for RMPs 21 and 25. Color transition from gray to black signals increase in x/C .

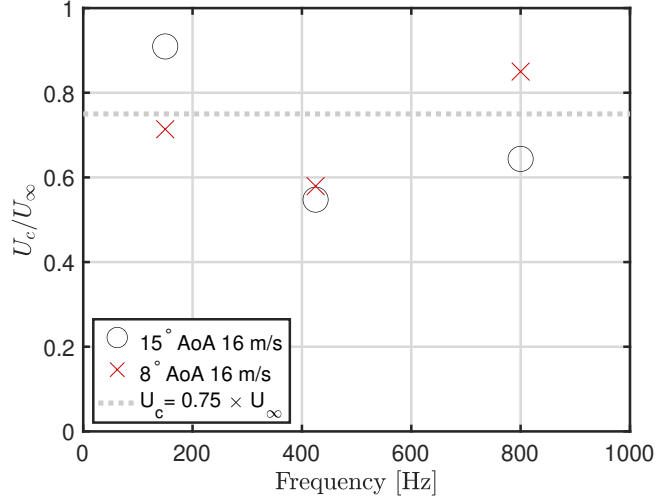


FIG. 7. Convection velocity (U_c) measured between RMPs 23 and 24. Dotted grey line is Moreau and Roger's (2005) mean estimate of U_c for 15° angle of attack and 16 m/s case.

by Kalyani, Moreau, and Ragni [2022] for this frequency range ($0.52 U_\infty$). Note that the observed variations can be caused by the uncertainty in the estimation of U_c , which should be a function of total recording time of the signal as shown in the appendix. In the low frequency ranges below 400 Hz, an increase in convection velocity is observed for the 15° angle-of-attack case compared to the 8° angle-of-attack case. This result is quite surprising, as an increase in adverse pressure gradient leads to a decrease in convection velocity [see, for instance, Schloemer 1967]. Therefore, this observation will be addressed in the subsequent

sections. Nevertheless, at higher frequencies beyond 400 Hz, the convection velocity for the 15° angle-of-attack case does become lower than that for the 8° angle-of-attack case. Finally, the convection velocity decreases with an increase in frequencies because at low frequency, only the large eddies contribute to the pressure gusts [see, for instance, Schloemer 1967]. At higher frequencies, the contribution from smaller eddies, which are close to the wall, becomes significant, resulting in lower convection velocities. Therefore, Schloemer [1967]’s observation regarding the frequency dependence of convection velocity is valid for both angles of attack.

Lastly, quantifying the spanwise correlation length is anything but straightforward. Corcos [1964], under the assumption that the normalized cross-power spectral density can be represented by two separate dimensionless variables $\omega\Delta x_1/U_c$ and $\omega\Delta x_3/U_c$, showed that the two-dimensional coherence function can be written as follows:

$$\gamma(\Delta x_1, \Delta x_3, \omega) = \frac{\Phi_{pp}(\omega, \Delta x_1, \Delta x_3)}{\Phi_{pp}(\omega, 0, 0)} = A(\omega\Delta x_1/U_c) B(\omega\Delta x_3/U_c) e^{-i\omega\Delta x_1/U_c} \quad (2)$$

The magnitude-squared coherence in the spanwise direction, is obtained by multiplying $\gamma(0, \Delta x_3, \omega)$ by its complex conjugate, and is plotted in figure 8 (a). As can be seen in the latter, the coherence goes to zero beyond 1000 Hz, which makes the estimation of the associated length scales impossible. More importantly, a hump centred around ~ 100 Hz is observed in the values of γ^2 . These results are consistent with the previous measurements by Moreau and Roger [2005] shown as symbols in figure 8 (a). Even though similar results were also reported by Kalyani, Moreau, and Ragni [2022] beyond 100 Hz, the oscillatory behavior observed in their figure 4 below 100 Hz is caused by a too short signal length as shown in the appendix.

Corcos [1964] was also first to recognize the exponential decay nature of the wall-pressure correlation separated by a finite distance, as also evidenced in figure 8 (a). Invoking observation of exponential decay of correlation made by Corcos [1964], the function A and B can be written as:

$$A(\omega\Delta x_1/U_c) = e^{-\omega b_2 \Delta x_1/U_c} \quad \text{and} \quad B(\omega\Delta x_3/U_c) = e^{-\omega b_1 \Delta x_3/U_c} \quad (3)$$

where, b_1 and b_2 are fitting parameters. Under the assumption of zero streamwise separation, the normalized cross-power spectral density can then be written as follows:

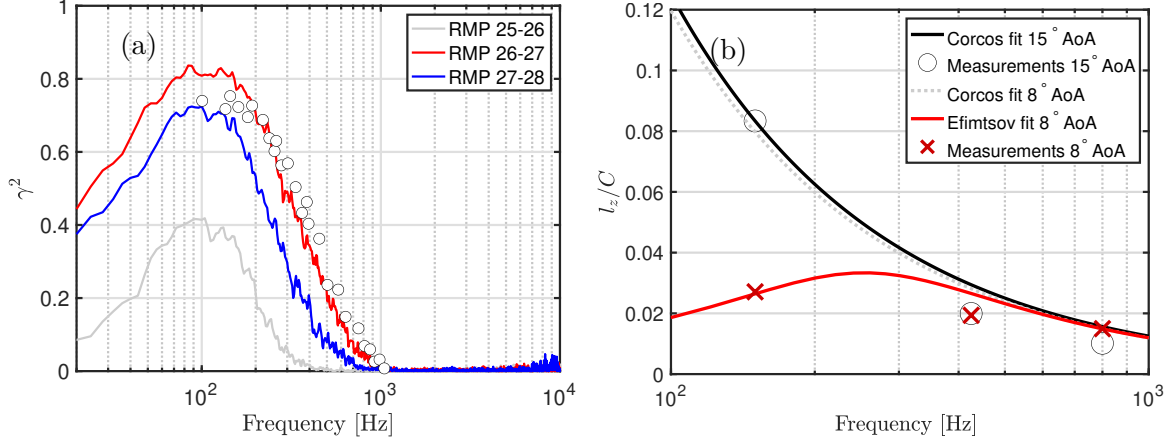


FIG. 8. Analysis of the spanwise wall-pressure at $U_\infty = 16$ m/s (a) Magnitude squared coherence (γ^2). Black circles for ECL measurements [Moreau and Roger 2005] for γ^2 between RMP 26-27. (b) Estimation of spanwise correlation lengths.

$$\gamma(0, \Delta x_3, \omega) = e^{-\omega b_1 \Delta x_3 / U_c} \quad (4)$$

The spanwise correlation length $l_z(f)$ can be estimated by:

$$l_z(\omega) = \int_0^\infty \gamma(0, \Delta x_3, \omega) \Delta x_3 \quad (5)$$

Plugging equation (4) in equation (5) yields:

$$l_z(\omega) = b_1 U_c / \omega \quad (6)$$

The reader should be cautioned that Corcos's model (equation (6)) can lead to nonphysical values of spanwise correlation length, as it relies on the assumption that the convection velocity is independent of frequency. Nevertheless, it provides a reasonable estimation of the correlation length and has been used in the past by several authors [Roger and Moreau 2004]. Therefore, Corcos's model (equation (6)) was used to estimate the spanwise correlation length. However, as the frequency at which the model should be used is unclear, the frequency was arbitrarily chosen. The resulting lengths are shown as the solid black and broken grey lines for the 15° angle-of-attack and the 8° angle-of-attack cases, respectively. The resulting values for the constant b_1 are 1.37 and 1.34 for the 15° and the 8° angle-of-attack cases, respectively. Although the estimate of Corcos's model predicts high-frequency attenuation in spanwise correlation length, it over-predicts it at low frequency for the 8°

angle-of-attack case. This can be corrected by using Efimtsov [1982] model (solid red line), which takes the boundary-layer thickness (δ) and friction velocity (u_τ) into account to re-scale correlation length in the low-frequency range. The three empirical constants were set to 1.34, 19.5, and 13.5 in order to estimate the spanwise correlation length with Efimtsov [1982] model.

In order to experimentally estimate the spanwise correlation length, the spanwise coherence between several spanwise sensors (RMPs 25 – 28) near the trailing edge ($x/C = 0.98$) was calculated. The estimated values of the real part of the coherence were fitted with an exponential decay function for a given frequency. The exponential decay function was chosen based on observations by Corcos [1964]. Finally, the correlation length l_z was obtained by combining equations (4) and (5). The resulting values of the correlation lengths ($l_z(f)$) are represented by symbols (crosses and circles) in figure 8 (b). As in the case of convection velocity, the spanwise correlation length also increases for the 15° angle of attack compared to the 8° angle of attack case. As wall pressure is an imprint of turbulent flows convecting over the surface, what flow structures can explain such an increase in convection velocity? To answer this question, velocity field measurements were carried out using PIV and will be discussed in the following section.

B. Velocity measurements

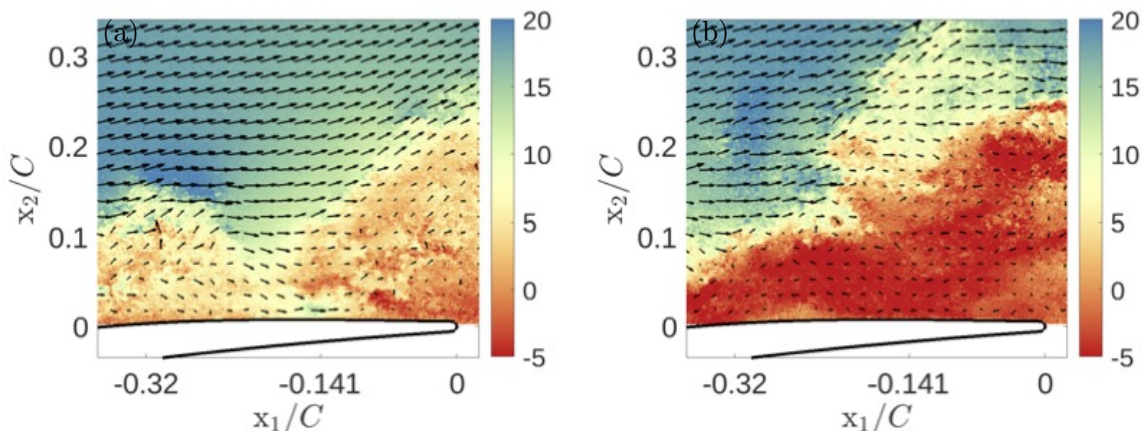


FIG. 9. Snapshots of instantaneous wall-parallel velocity at two time instants.

Two snapshots of wall-parallel velocity are plotted in figure 9. As can be seen, large rollers, similar to that reported by Jaiswal *et al.* [2022] at 5° incidence, are observed, which

evidences the presence of large coherent structures. This is also consistent with the flow topology seen by Christophe and Moreau [2008] in their LES at 15° . These structures are typically induced by instability within the separated shear layer. At some instant, even a fully separated boundary-layer is observed as shown in figure 9 (b). These instantaneous flow fields confirm large scale separation and passage of coherent rollers at the trailing edge, which are reminiscent of Kelvin-Helmholtz flow type.

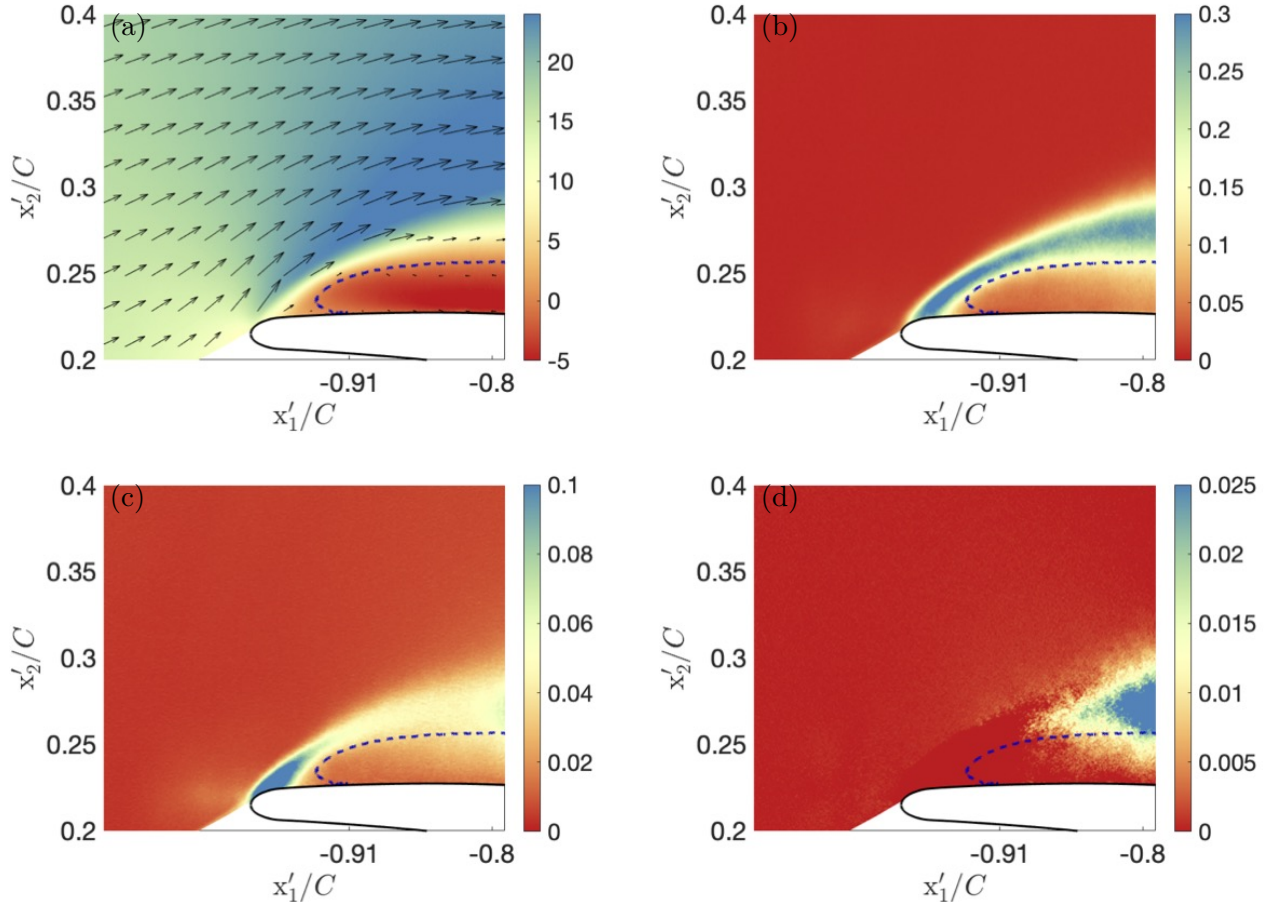


FIG. 10. Contours of velocity statistics over the airfoil leading edge (blue dashed lines are the iso-contours of zero wall-parallel velocity U_∞): (a) mean wall-parallel velocity U_1 ; (b) $\frac{\overline{u_1^2}}{U_\infty^2}$; (c) $\frac{\overline{u_2^2}}{U_\infty^2}$; (d) $-\frac{\overline{u_1 u_2}}{U_\infty^2}$. Coordinate system is aligned with the leading edge.

Figures 10 and 11 show the mean boundary-layer statistics recorded by the first and the second camera, respectively. Figure 10 is plotted with respect to an observer sitting on the leading-edge of the airfoil while in figure 11, the coordinate system of the velocity field is aligned with the wind-tunnel axis. As evidenced in table II, the spatial resolution achieved by the first camera is about three times higher than that of the second camera. Thus, further

spatial filtering is expected in the results shown in figure 11. Figure 10 shows that, in a time-averaged sense, the mean flow becomes separated from RMP 3 ($x/C = 0.09$) onward. This is consistent with figure 3, which shows a plateau in C_p between RMP 3 and RMP 6. More importantly, the separated region shown by the black dashed lines in figures 10 and 11 has a negligible r.m.s value of velocity disturbances (all Reynolds stresses close to zero). This confirms the laminar nature of the time-averaged separated flow region, and in the literature, it is commonly referred to as the LSB. The presence of such an LSB is characteristic of the flow past the CD airfoil at $Re_c = 150000$ and is consistent with the finding of Christophe and Moreau [2008], who also reported the presence of a LSB when the CD airfoil is placed at a 15° incidence. The LSB near the leading-edge of the airfoil seems to deflect the mean flow away from the airfoil, which provides a possible explanation for a drop in mean-loading reported in figure 3. The deflected mean flow and resultant flow acceleration near the leading-edge, at the point of inception of the LSB, can be evidenced from an increase in the length of arrows in figure 10. In a time-averaged sense, the LSB seems to cover at least 30% of the airfoil chord. However, due to the limited field-of-view, the exact extent of the LSB could not be quantified. Overall, the mean flow topology presented in figures 10 and 11 show that the flow at the leading-edge region of the CD airfoil at 15° angle of attack and $Re_c \simeq 150000$ is laminar in nature. The LSB ensures the flow transition that occurs only after $x/C > 0.4$ as found in the previous LES [Christophe and Moreau 2008].

The mean boundary-layer statistics recorded by the third camera are shown in figure 12 for the case when the airfoil is placed at a 15° angle of attack with an inlet velocity of 16 m/s. Figure 12 (a) shows the mean wall-parallel velocity. Despite the large-scale flow separations observed in figure 9, the boundary-layer near the trailing edge is fully attached in a time-averaged sense. As such, in the present pre-stall noise study, the time-averaged flow near the trailing-edge of the CD airfoil is different from the one reported by Lacagnina *et al.* [2019], who reported a separated time-averaged flow near the trailing edge. The black dotted line is the iso-contour of the inlet velocity free-stream velocity, which roughly corresponds to the overall extent of the boundary layer. The Reynolds stress tensor terms, $\overline{u_1 u_1}/U_\infty^2$, $\overline{u_2 u_2}/U_\infty^2$, and $-\overline{u_1 u_2}/U_\infty^2$, are shown in figures 12 (b), (c), and (d), respectively. Compared to the leading-edge region, the disturbances (quantified by r.m.s of velocities) close to the trailing-edge are substantially higher, which implies that the flow transitions

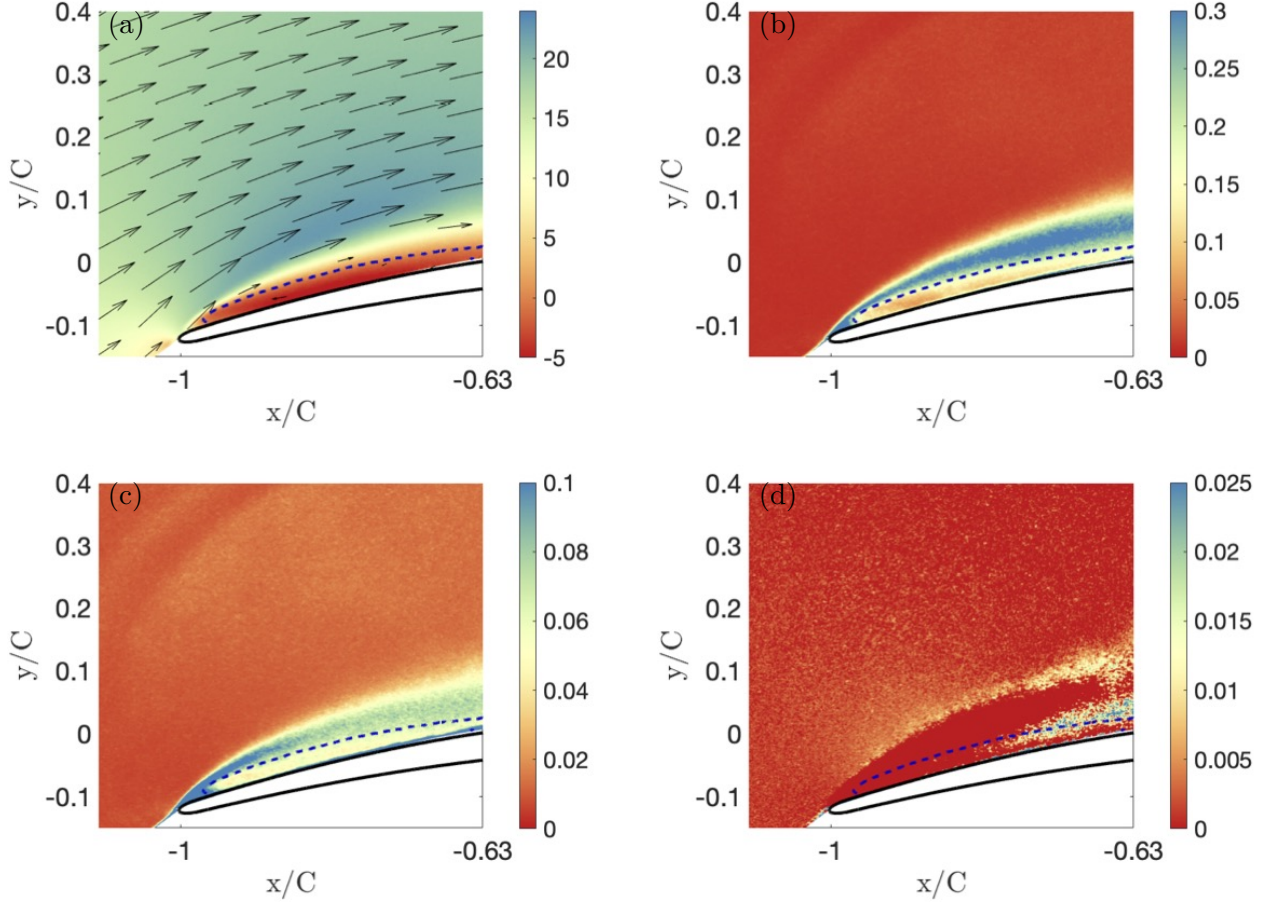


FIG. 11. Contours of velocity statistics over the airfoil leading edge (blue dashed lines are the iso-contours of zero wall-parallel velocity U_∞): (a) mean wall-parallel velocity U_1 ; (b) $\frac{\overline{u_1 u_1}}{U_\infty^2}$; (c) $\frac{\overline{u_2 u_2}}{U_\infty^2}$; (d) $-\frac{\overline{u_1 u_2}}{U_\infty^2}$. Coordinate system is aligned with the leading edge.

to a fully turbulent boundary-layer somewhere between 40 and 65% of the chord. Higher levels of r.m.s velocities are the sources of far-field noise [Ffowcs Williams and Hall 1970]. In particular, elevated regions of r.m.s velocity do not have a clear peak but a broad region of elevated intensity. This is typical of flows that experience the presence of shear-layer instabilities [Jaiswal *et al.* 2022].

In order to understand the impact of the Reynolds number, the results of the measurements performed at 28 m/s are plotted in figure 13. Upon comparison with figure 12, it shows similar overall behavior in the measured velocity field in the trailing-edge region. The overall length of the boundary layer is similar to the 16 m/s case at $x_2 \simeq 0.32 C$ and close to the trailing-edge region ($x_2 \simeq 0.02 C$), as shown in tables III and IV. Furthermore, for the 28 m/s case, the turbulence intensity appears to be much lower than in the 16 m/s case,

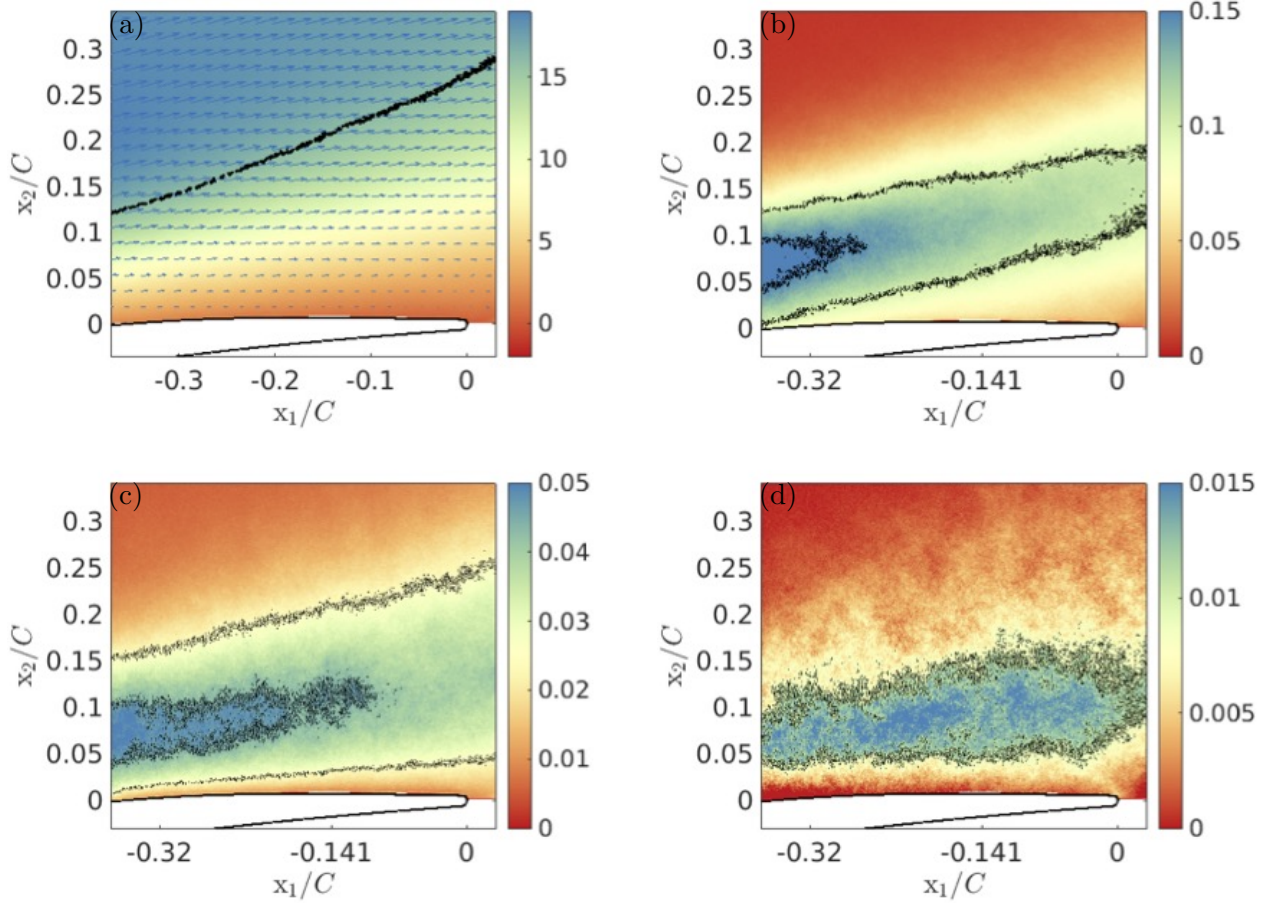


FIG. 12. Contours of velocity statistics over the airfoil trailing edge for $U_\infty = 16$ m/s: (a) mean wall-parallel velocity U_1 (black line corresponds to free-stream inlet velocity U_∞), (b) $\frac{\overline{u_1 u_1}}{U_\infty^2}$ (black dashed lines indicate iso-values of 0.15 and 0.1); (c) $\frac{\overline{u_2 u_2}}{U_\infty^2}$, black dashed lines indicate iso-values of 0.045 and 0.025; (d) $-\frac{\overline{u_1 u_2}}{U_\infty^2}$, black dashed line indicates iso-values of 0.01. Coordinate system is aligned with the trailing edge.

resulting in more localized levels of iso-contours in figure 13 compared to those in figure 12. This is especially true for the cross-term $-\overline{u_1 u_2}/U_\infty^2$.

A more quantitative comparison can be obtained by looking at the velocity profiles near the airfoil trailing edge, as shown in Figure 14. The velocity profile at RMP 26 ($x/C = 0.98$) shows when the CD airfoil placed at 15° and 16 m/s flow incidence and inlet velocity respectively, the near wall mean velocity is reduced compared to the inlet velocity. Similar observations have been made by Caiazzo *et al.* [2023] (see figure 4), who reported a decrease in the near wall mean velocity as the mean pressure gradient increases. As such, we expect the boundary layer to grow faster in the streamwise direction near the trailing-edge region

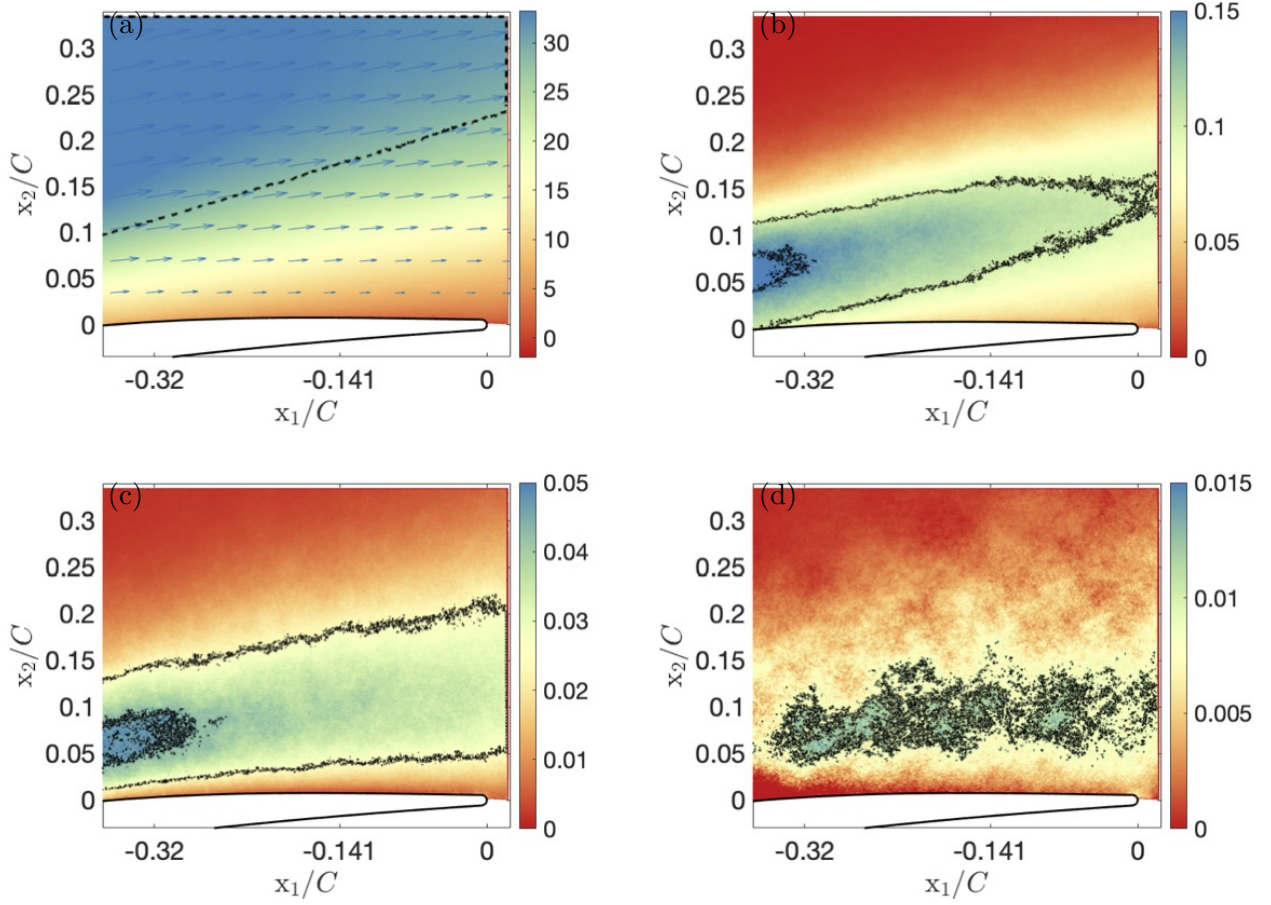


FIG. 13. Contours of velocity statistics over the airfoil trailing edge for $U_\infty = 28$ m/s: (a) mean wall-parallel velocity U_1 (black line corresponds to free-stream inlet velocity U_∞), (b) $\frac{\overline{u_1 u_1}}{U_\infty^2}$ (black dashed lines indicate iso-values of 0.15 and 0.1); (c) $\frac{\overline{u_2 u_2}}{U_\infty^2}$, black dashed lines indicate iso-values of 0.045 and 0.025; (d) $-\frac{\overline{u_1 u_2}}{U_\infty^2}$, black dashed line indicates iso-values of 0.01. Coordinate system is aligned with the trailing edge.

for the 28 m/s case compared with the 16 m/s case. This faster growth of the boundary layer for the 28 m/s case is captured in the shape factor, which remains smaller at both RMP 21 and RMP 26 locations compared to 16 m/s (see the values in Tables III and IV, for instance). Yet, both velocity cases have higher values of the shape factor compared to the case when the airfoil is fixed at 8° angle of attack and 16 m/s. Notably, a higher value of the shape factor indicates flow close to separation [see Figure 10 of Sanjose *et al.* 2019]. Therefore, as the flow speed increases, the probability of flow separation decreases. Nevertheless, the overall boundary layer extent is similar for the 28 m/s and 16 m/s cases, as evidenced in Tables III and IV. As such, the Reynolds number based on the momentum

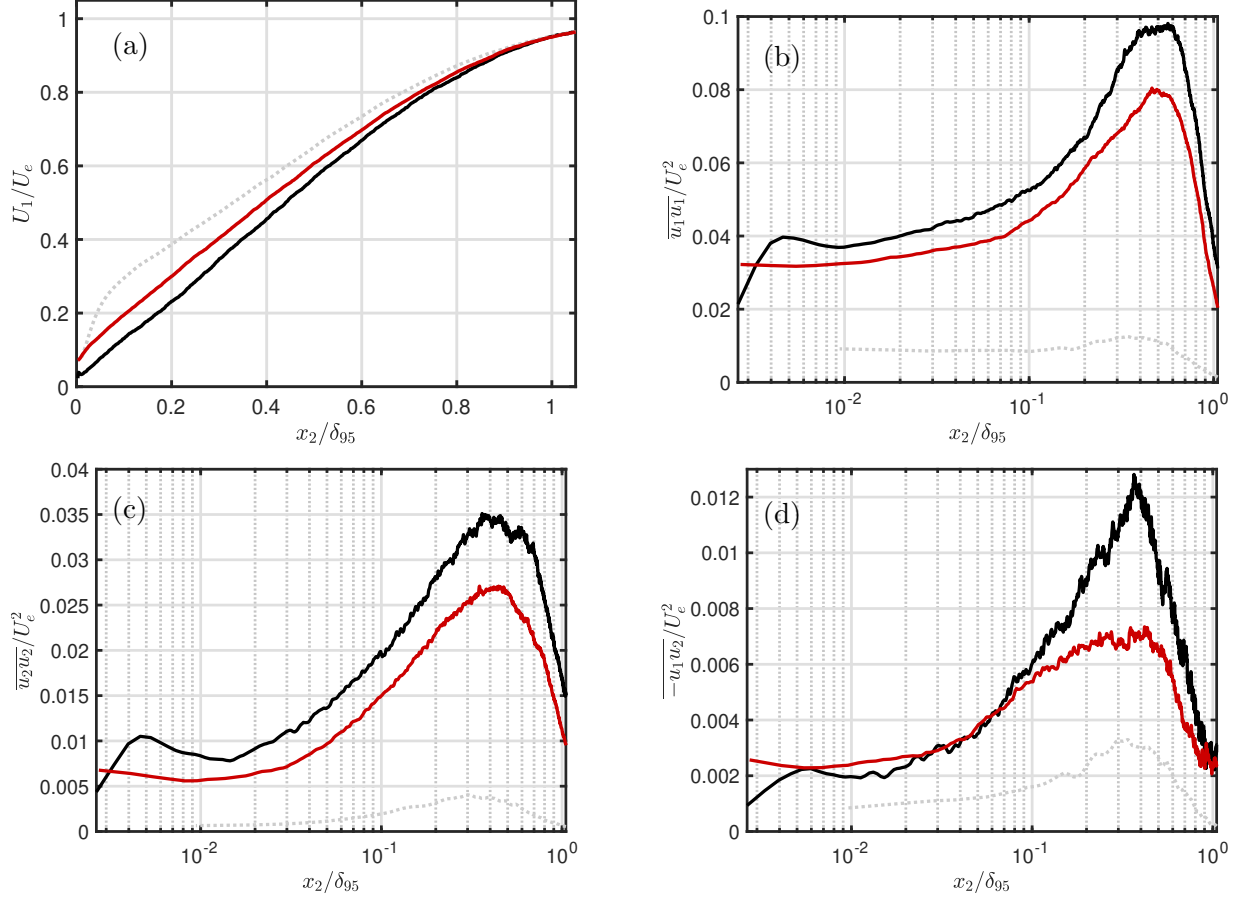


FIG. 14. Comparison of velocity profiles at RMP 26 ($x/C = 0.98$). Legend: Solid black and red lines correspond to airfoil placed at 15° angle-of-attack and at an inlet velocity of 16 and 28 m/s respectively. Dotted grey line corresponds to airfoil placed at 8° angle-of-attack and at an inlet velocity of 16 m/s.

thickness (Re_θ) for the airfoil placed at 15° angle-of-attack is substantially higher than that of the 8° case near the trailing-edge region. The profiles of velocity statistics, namely $\overline{u_1 u_1}/U_\infty^2$, $\overline{u_2 u_2}/U_\infty^2$, and $-\overline{u_1 u_2}/U_\infty^2$, for the two velocity cases at 15° angle of incidence and the case when the airfoil is placed at 8° angle of attack and $U_\infty = 16$ m/s are compared in figures 14 (b-d). Generally, the velocity statistics are normalized with the friction velocity to remove any Reynolds number (Re_τ) based effects. However, the overall goal of plot 14 (b-d) is to demonstrate the levels of velocity disturbances with respect to the inlet velocity U_∞ . Such a scaling inherently shows the applicability of thin-airfoil linearized theory, which assumes that the velocity disturbances are small compared to the inlet velocity U_∞ . While the peak levels of velocity statistics scale with the boundary-layer thickness δ_{95} , in absolute

TABLE III. Boundary layer parameters at RMP 21 ($x/C = 0.8582$)

AOA	U_∞	U_e	δ_{95}	δ^*	θ	H	Re_θ	$-\overline{u_1 u_{2max}}$	$\frac{p_{rms}}{-\rho \overline{u_1 u_{2max}}}$
	[m/s]	[m/s]	[mm]	[mm]	[mm]			[m ² /s ²]	
8°	16	18.7	4.41	1.36	0.82	1.65	997	0.77	2.6
15°	16	17.81	28.97	12.73	5.06	2.51	5847	4.01	3.08
15°	28	32.8	28.61	11.53	5.25	2.19	11188	8.68	—

TABLE IV. Boundary layer parameters at RMP 26 ($x/C = 0.98$)

AOA	U_∞	U_e	δ_{95}	δ^*	θ	H	Re_θ	$-\overline{u_1 u_{2max}}$	$\frac{p_{rms}}{-\rho \overline{u_1 u_{2max}}}$
	[m/s]	[m/s]	[mm]	[mm]	[mm]			[m ² /s ²]	
8°	16	17.44	6.34	2.42	1.19	2.03	1350	1	2.77
15°	16	17.15	34.88	16.16	6.03	2.67	6712	3.76	2.22
15°	28	31.88	33.78	14.35	6.088	2.35	12577	7.46	—

units (for instance in meters) they are much further away from the wall compared to the 8° angle-of-attack and 16 m/s case. More importantly, the profiles confirm that the r.m.s levels of velocity disturbances are elevated for the CD airfoil placed at 15° angle-of-attack at 16 m/s case compared to the rest. With the exception of the wall-parallel disturbances ($\overline{u_1 u_1}/U_\infty^2$) for the 15° angle-of-attack at 16 m/s case, the disturbances are at least an order of magnitude smaller in the rest of the cases tested. Previous studies [see figure 9 of Caiazzo *et al.* 2023, for instance] have reported an increase in r.m.s levels of velocity disturbances for wall bounded flows subjected to mean adverse pressure gradients.

Recently, Pargal [2023] showed that normalizing the wall-pressure spectra by the square of the maximum value of the Reynolds stress, denoted by $|\overline{u_1 u_2}|_{max}^2$, leads to a collapse in low-frequency spectra over a broad range of cases for boundary-layer flows subjected to arbitrary mean pressure gradient. This normalization holds true because, as first shown by Na and Moin [1998], the term $p_{rms}/(-\rho \overline{u_1 u_{2max}})$ falls between 2 and 3 for boundary-layer flows. This was later confirmed by [Abe 2017; Le Floc’h *et al.* 2020] for canonical boundary-layer flows, and more recently by Caiazzo *et al.* [2023] for flows past an airfoil. These

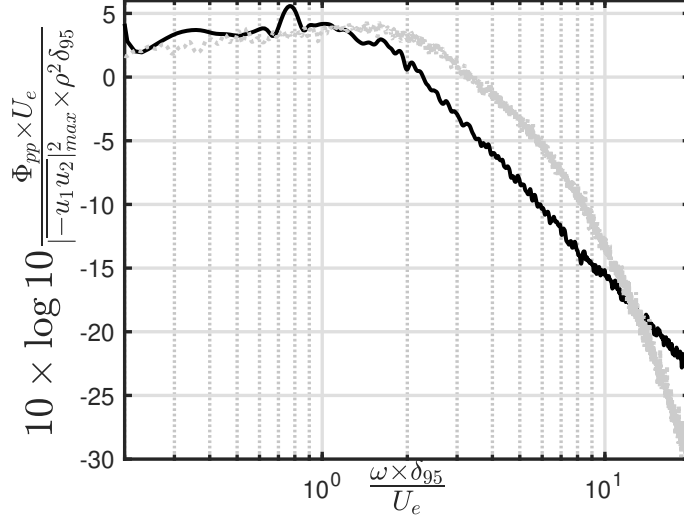


FIG. 15. Power spectral density of the wall-pressure fluctuations at RMP 26 at fixed inlet velocity $U_\infty = 16$ m/s. The PSD has been normalized by the maximum value of the square of $-\overline{u_1 u_2}$, the square of the free-stream density ρ , the local edge velocity U_e and the boundary-layer thickness δ_{95} . Legends: Dotted grey line for CD airfoil at an incidence of 8° while solid black line represents CD airfoil at an incidence of 15° .

observations are confirmed in tables III and IV for the present case. Small deviations from the aforementioned values can be ascribed to measurement uncertainty, and the presence of open jet, which predominantly contributes to low frequency wall-pressure spectra and which is absent in the aforementioned data [Abe 2017; Caiazzo *et al.* 2023; Le Floc’h *et al.* 2020; Pargal 2023]. More importantly, when the scaling proposed by Pargal [2023] is used to scale the wall-pressure spectra in Figure 15, a collapse in the low-frequency range is achieved. This collapse is remarkable because the wall-pressure spectra exhibit a difference of 20 dB, as shown in Figure 6, corresponding to an order of magnitude difference in wall-pressure fluctuations.

As the PIV velocity measurements were not time-resolved, additional single wire measurements were performed. As mentioned, single HWA measurements were performed close to the trailing-edge (RMP 26) of the airfoil. These measurements were done for airfoil placed at 15° angle of attack and fixed inlet velocity of $U_\infty = 16$ m/s. Figure 16 shows the pre-multiplied spectrogram $f \times E_{11}/U_e^2$. The plot shows that the pre-multiplied energy spectrum peaks at about 100 Hz, away from the wall ($0.4 - 0.6 \times \delta_{95}$), approximately the location where the peak in r.m.s. of velocity fluctuations was reported in figure 14.

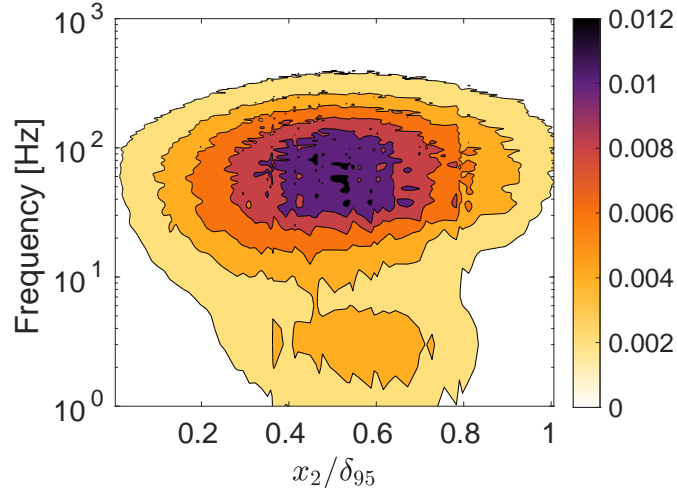


FIG. 16. Premultiplied 1-D velocity energy spectra $\overline{E_{11}} (f \times E_{11}/U_e^2)$ as a function of frequency, over the airfoil at RMP 26.

In summary, figures 14 to 16 show that large scale flow disturbances may be present and confirm the instantaneous snapshots in figure 9. These large structures are in turn responsible for elevated levels of r.m.s. velocity fluctuations and the peak in the pre-multiplied spectrogram. As such, modal decomposition could be useful to understand the hierarchy and the organization of velocity disturbances close to the trailing edge.

IV. MODAL ANALYSIS

The Proper Orthogonal Decomposition (POD) [Holmes *et al.* 2012] was employed to uncover the modes present in the velocity disturbance field. One benefit of using POD is that, unlike linear stability analysis, it does not require velocity disturbances to be small. In the present paper, POD was carried out using the snapshot approach of the algorithm developed by Sirovich [1987]. For more information, please refer to the monograph by Holmes *et al.* [2012]. The modal energy distribution of the measured velocity field is shown in figure 17. The spatial POD modes are used to identify the spatial organization of the velocity disturbance field and their associated energy levels (E_r), and are plotted in figure 18. In the present manuscript, only the spatial modes associated with the vertical velocity disturbances (E_{22}) are used because they are the principal drivers of wall-pressure fluctuations and far-field acoustics [Jaiswal *et al.* 2020]. Figure 17 (b) clearly shows that the first 12 modes

contribute to approximately 40% of the total energy, although the cumulative energy for the 16 m/s case appears to be slightly lower compared to the 28 m/s case. The relative contributions for the 16 m/s and 28 m/s are shown for the first 12 modes. As can be seen, the relative energies of modal pairs 3-4, 5-6, and 11-12 appear to be similar and may form a modal pair. However, upon inspection, it was found not to be the case (see figure 18 for example). Yet, the spatial organization appears to be similar between the 16 m/s and 28 m/s cases. Moreover, in these figures, the dashed black lines that represent the time-averaged location where the wall-parallel velocity is equal to the free-stream velocity U_∞ show that the spatial modes are distributed across the boundary layer. In contrast, modal decomposition performed by Lacagnina *et al.* [2019] had shown that the spatial modes are uniquely present outside the time-averaged extent of the shear layer. In fact, the spatial distribution of the velocity disturbance field looks similar to the instantaneous field in figure 9 (a), and it could be due to the passage of coherent structures, and it may correspond to the disturbance at the frequency range of 80 – 300 Hz. More importantly, the spatial extent or wavelength of this modal pattern (mode 3) closely corresponds to the peak in the pre-multiplied spectrogram (figure 16). As such, it may be responsible for the hump in the low-frequency wall-pressure (figure 6) and far-field acoustic spectra (figure 4). To verify this, the correlation between mode 3 and band-passed pressure will be performed next.

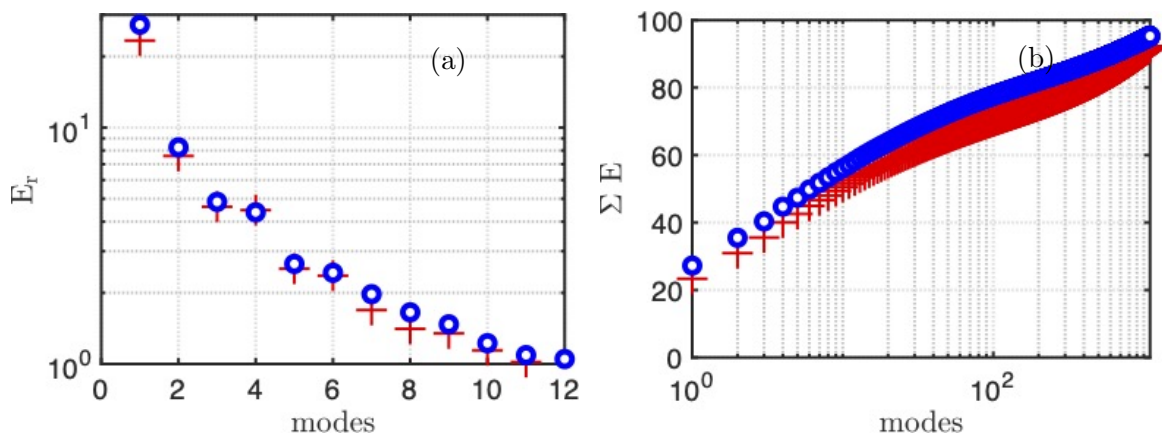


FIG. 17. POD based modal decomposition of the measured velocity field in the trailing-edge region (camera 3) for an airfoil placed at 15° angle of attack. (a) Relative energy of individual POD modes; (b) Cumulative sum of POD modes. Legends: Red cross for inlet velocity of $U_\infty = 16$ m/s while the blue circles represent inlet velocity of $U_\infty = 28$ m/s.

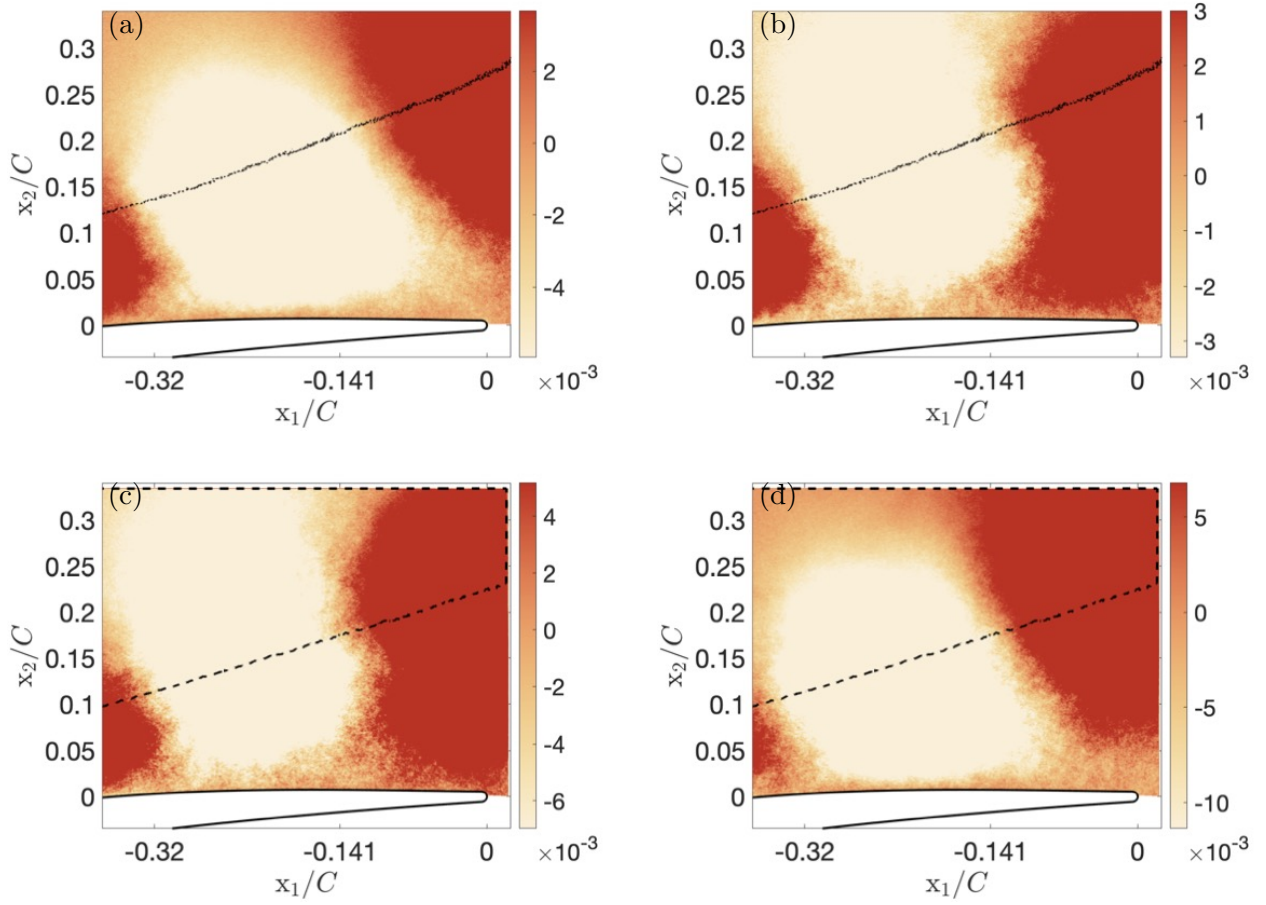


FIG. 18. Modes of the vertical velocity disturbances, E_{22} , measured at the trailing-edge of the airfoil. Coordinate system is aligned with the trailing edge. Left plots (a) and (c) correspond to mode 3 while right ones are for mode 4. Top figures (a) and (b) correspond to $U_\infty = 16$ m/s while bottom figures correspond to $U_\infty = 28$ m/s. Black contour lines show the corresponding mean free-stream inlet velocity U_∞ .

V. CORRELATION ANALYSIS

Having characterized the velocity and pressure field, the manuscript will now attempt to delineate the correlation between these two quantities of interest. Correlation between flow quantities are quantified using Pearson's correlation coefficient. Pearson correlation coefficient at two different locations (x_1, x_2, x_3) and (x_1', x_2', x_3') is denoted by:

$$R_{\zeta\chi}(x_1, x_1', x_2, x_2', x_3, x_3') = \frac{\overline{\zeta(x_1, x_2, x_3)\chi(x_1', x_2', x_3')}}{\sqrt{\overline{\zeta(x_1, x_2, x_3)^2}} \times \sqrt{\overline{\chi(x_1', x_2', x_3')^2}}} \quad (7)$$

where $\zeta(x_1, x_2, x_3)$ and $\chi(x_1', x_2', x_3')$ are the fluctuating components of variables of interest.

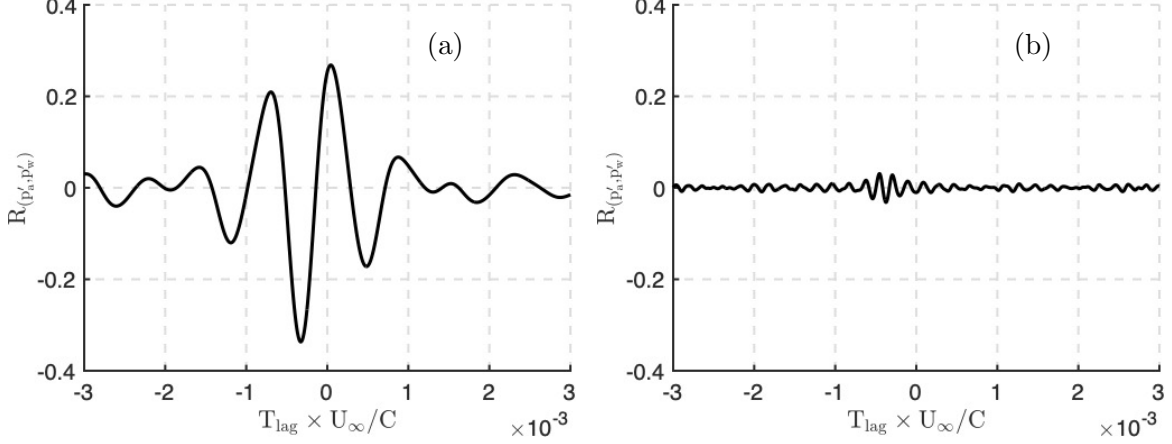


FIG. 19. Cross-correlation between filtered wall-pressure and far-field pressure for 15° angle-of-attack and $U_\infty=16$ m/s. (a) Cross-correlation for pressure signals filtered between 100-300 [Hz]; (b) Cross-correlation for pressure signals filtered between 600-2100 [Hz].

The Pearson correlation method is used in pattern recognition to quantify the similarity between patterns or features in data. For example, in time series data, the correlation between the values of two time series at different time points can be used to quantify the similarity between the patterns of the time series. However, correlation alone does not establish causation, as correlation cannot yield causal asymmetry and hence cannot separate the cause from the effect [Bossomaier *et al.* 2016]. As such, in the present section the overall goal is recognize pattern in velocity disturbance field that are *similar* to ones measured in time series of pressure signals recorded at the wall or at far-field locations. This can aid to identify velocity disturbance pattern associated with separation noise. The causality is inferred through Amiet’s (1976) equation (1) and Poisson’s equation [see Grasso *et al.* 2019, for instance], which relates velocity disturbance to wall-pressure fluctuations.

A. Wall and far-field pressure correlation analysis

To identify patterns in measured time series of wall-pressure and far-field acoustic pressure the correlation, $R_{p'_w, p'_a}$, has been calculated. To segregate the separation noise, both signals have been band-passed filtered between 80 – 300 Hz and 600 – 2100 Hz, where contributions from separation noise can be ignored (see figure 16). The results are shown in figures 19 (a-b). A negative correlation between the wall-pressure fluctuations p'_w and the far-field acoustic ones p'_a is measured when these signals have been band-passed filtered between 80 – 300.

This can be caused by the passage of eddies at these frequencies near the trailing-edge and their diffraction in the form of acoustic pressure at a far-field location (see also figure 16). The phase opposition between near-field and far-field is due to the dipole nature of the source term. In contrast, for the band passed frequencies between 600 – 2100 Hz, no meaningful correlation is obtained. This already suggests a significant low-frequency contribution of the surface noise sources caused by the largest turbulent coherent structures.

B. Correlation between POD modes and pressure

The temporal signals associated with mode 3, has been correlated with the band-passed filtered wall-pressure and far-field pressure signals. The frequency band for the separation noise has been chosen to be between 80 – 300 Hz and 600 – 2100 Hz, as in figure 19. Once again the band passed filtering has been achieved using a zero-phase digital filtering, which conserves the phase. Figures 20 (a) and (b) show the correlation between the third mode (R_{E_{22},p'_w}) and the wall-pressure fluctuations measured by RMP 26 ($x/C = 0.98$). In these plots, T_f corresponds to the time of flight of an acoustic signal emitted at the trailing-edge of the airfoil to reach the far-field location where the noise is measured. The third mode of wall-normal velocity fluctuations (E_{22}) and the recorded wall-pressure signals p'_w show a meaningful correlation only at the band-pass frequency range of 80 – 300 Hz (figure 20 (a)), while the correlation drops to background noise levels for the higher frequency band 600 – 2100 Hz (figure 20 (b)). Similarly for the correlation between mode 3 and the far-field acoustic pressure p'_a meaningful results are only obtained for the lower frequency band 80 – 300 Hz. The only difference is that it takes the near field hydrodynamic event a finite time to reach the far-field location, where the acoustic measurements are achieved. As such, before the cross-correlation was performed, the time series of the acoustic signal was shifted by the time of flight T_f . More importantly a phase opposition is seen in figure 20 (c)) between mode 3 and the far-field acoustic pressure. This is not surprising as the third mode of the wall-normal velocity disturbances (E_{22}) and the recorded wall-pressure signals are in phase (see figure 20 (c)) while the acoustic pressure and wall-pressure field are in phase opposition (figure 19).

To conclude, the near-field source terms are amplified in the case when the airfoil is placed at high angles of attack through induced flow separation. The separated shear layer

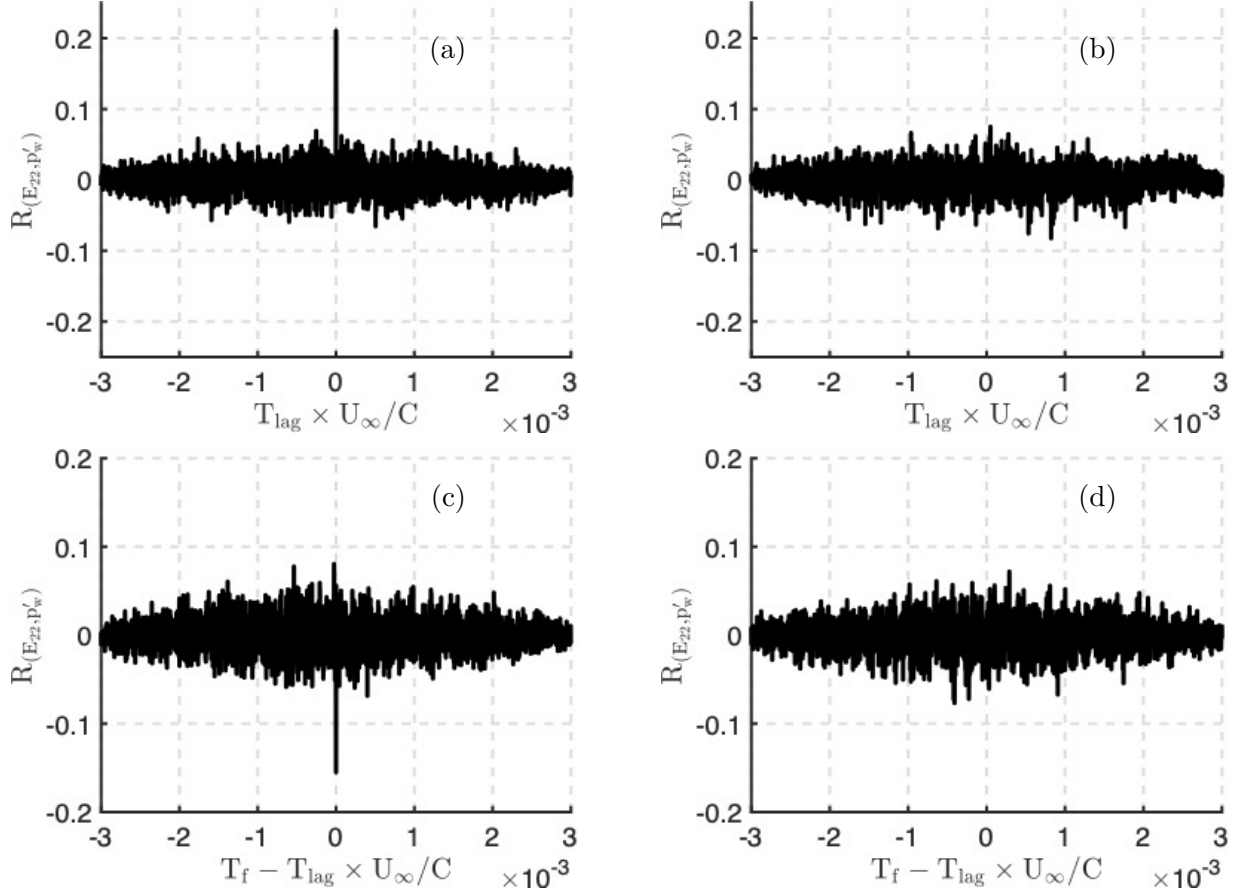


FIG. 20. Cross-correlation between the third mode of wall-normal velocity fluctuations (E_{22}), filtered wall-pressure fluctuations p'_w and far-field acoustic pressure p'_a . Legends: (a) and (b) R_{E_{22}, p'_w} ; (c) and (d) R_{E_{22}, p'_a} . Left figures (a) and (c) correspond to pressure fluctuations band-passed filtered between 80 – 300 [Hz] while right figures correspond to pressure fluctuations band-passed filtered between 600 – 2100 [Hz].

can induce Kelvin-Helmholtz like roller structures, the imprint of which are registered by the surface pressure probes. This results in an increased noise content, at a frequency that is associated with the wavelength of these roller structures. Having characterized the near-field source terms and its correlation with far-field acoustics, the diffracted acoustic pressure field around the airfoil is then quantified. Finally attempts are made to identify the equivalent source images responsible for the separation noise.

VI. FAR-FIELD ACOUSTIC PRESSURE ANALYSIS

The far-field acoustic pressure has been measured around the airfoil mid-chord to compare the influence of angles of attack on the acoustic directivity patterns. This has been done at several frequencies, and hence at several Helmholtz numbers kc , where k is the acoustic wavenumber. The results are shown in figure 21. While there is an overall increase in absolute levels of the measured sound pressure levels, the overall sound directivity pattern is similar between the 8° and 15° angles of attack cases, where the former is known to emit noise through an equivalent dipole at the trailing edge [Wu, Moreau, and Sandberg 2020]. As such, classical dipole noise at the airfoil trailing-edge seems to be the driver of separation noise. In contrast, at higher Mach numbers ($M_\infty = 0.3 - 0.4$) than the ones reported in present study, Turner and Kim [2022] had reported a significant contribution from the quadrupole noise sources.

To further investigate the overall contribution of quadrupole noise generated, due to separated shear layers, the cross-correlation between two far-field microphones located on either side of the airfoil mid-chord was performed. To isolate the influence of separation noise, the far-field noise signals were band-passed filtered between 80 and 1000 Hz. The comparison at 16 m/s between the two angles of attacks, 8° and 15° are shown in figure 22 (a). The clear phase opposition decisively demonstrates that the dominant noise source is dipolar in nature. To further reinforce these findings, the OverAll Sound Pressure Level (OASPL) as a function of free-stream velocity U_∞ is shown in figure 22 (b). Once again, to isolate overall influence of separation noise, the sound pressure levels have been integrated between 80 – 1000 Hz, where the separation noise dominates. The results clearly show that the OASPL due to noise separation follows the classical compact dipole scaling U_∞^6 , which was first proposed by Curle [1955].

Having shown that the separation noise can be represented by an equivalent compact dipole source, we now attempt to check whether it can be quantified using the diffraction theory outlined above in equation (1) [Amiet 1976]. The success of Amiet’s model and its extension relies on the fact that the response of the airfoil to an incident gust can be predicted using the linearized thin-airfoil theory. Following Moreau and Roger [2009]; Roger and Moreau [2004], the dimensionless radiation ratio Λ is plotted in figure 23. Red dashed lines correspond the frequency range for which the estimation of the spanwise correlation length

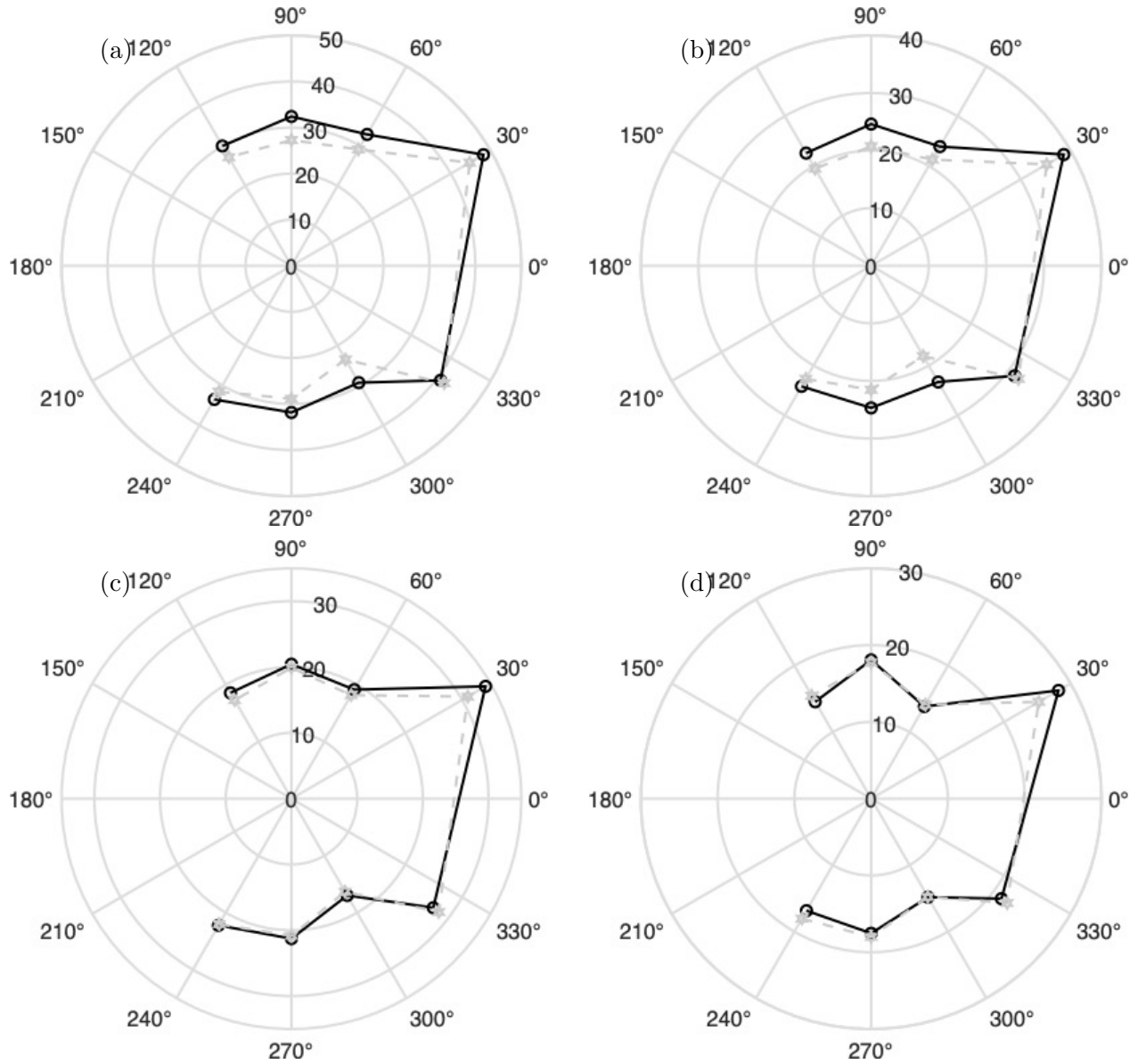


FIG. 21. Sound Pressure Level directivity measured at 1.21 m from the trailing-edge. Microphone locations are shown with respect to the wind tunnel axis. Solid black lines for airfoil at 15° Grey broken lines for airfoil at 8°. (a) 100 Hz ($kC = 0.24$) (b) 300 Hz ($kC = 0.74$) (c) 500 Hz ($kC = 1.23$) (d) 1000 Hz ($kC = 2.46$).

was performed. The high frequency region is limited to 1 kHz because the spanwise coherence for the 15° angle-of-attack case drops drastically below the measurement uncertainty beyond this frequency range. The radiation ratio quantifies the diffraction efficacy for an airfoil trailing-edge that is subjected to an unsteady pressure gust. To recall, the radiation ratio is defined as the ratio of far-field and near-field spectra normalised by spanwise length scales,

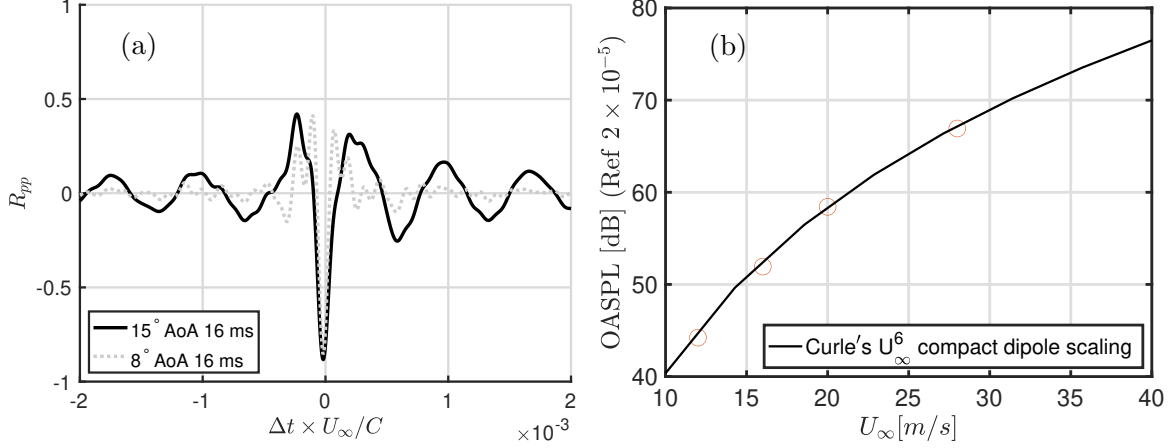


FIG. 22. Far-field sound pressure correlation and scaling at 15° . The sound pressure signals are filtered between 80 and 1000 Hz to single out flow separation contributions. (a) Cross-correlation between far-field microphones located perpendicular to airfoil chord. (b) OverAll Sound Pressure Level (OASPL) as a function of U_∞ .

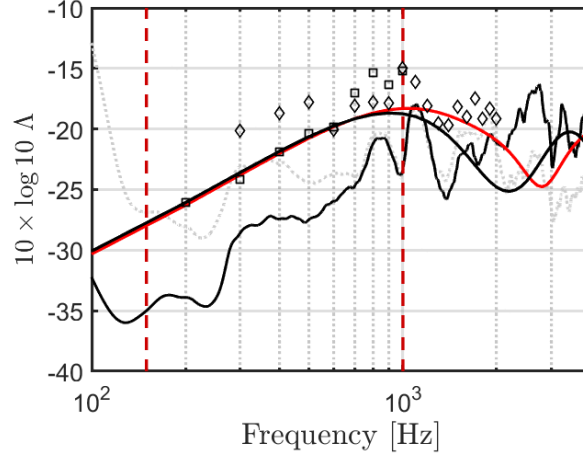


FIG. 23. Dimensionless radiation ratio at 16 m/s. Legend: Dotted and solid black line for 15° ; dotted gray line for 8° . Red dashed lines correspond the range where the experimental quantification of spanwise correlation was possible. Solid black and red lines are the theoretical predictions for an observer at 258° and 265° with respect to airfoil chord at a distance of 1.21 m. Hollow diamond and square correspond to measurements performed by Moreau and Roger [2005]

far-field observer distance and the airfoil span length, in the following manner:

$$\Lambda = \frac{S_{pp}}{\Phi_{pp} \times l_z} \times \frac{\mathbf{x}^2}{L} \quad (8)$$

As argued by Moreau and Roger [2009]; Roger and Moreau [2004], a good collapse between

various cases should be expected for the same airfoil. Figure 23 compares the present measurements with the theoretical prediction with Amiet’s model (solid lines) and the previous measurements at ECL (diamond and square symbols) as reported in Moreau and Roger [2009]. The two theoretical curves stress the effect of directivity in Λ and the actual microphone position in the present experiment, 258° (on the airfoil pressure side to provide laser access on the suction side), reproduces better the experimental trend compared to the ECL measurements at about 270° (or equivalently 90° on the airfoil suction side). The 5 dB spread in the experimental data is consistent with the data of figure 16 (a) in Moreau and Roger [2009], and can be attributed to both the saturation in the Electret microphones at low frequencies shown in figure 5 and a less accurate calibration methods in 2005. Yet, in both data sets, while a good collapse between the two angles of attack 15° and 8° is achieved between 500 and 2000 Hz, the collapse is relatively poor at lower frequencies (80 – 500 Hz range), for the high incidence where the separation noise dominates. On the other hand, the newer 8° case shows a good match with Amiet’s prediction.

VII. DISCUSSION

The low-frequency content of the airfoil self noise increases as the angle of attack is increased from 8° to 15° . This increase noise is also accompanied by an increase in the amplitude of wall-pressure and velocity disturbances.

The wall-pressure field shows an increased amplitude, spanwise extent and the velocity at which pressure gusts convect past the trailing-edge at frequencies where the separation noise is dominant. The genesis of the increased disturbances can be linked to the late transition of boundary layer. In particular, as the angle of attack is increased, it was found that the LSB covers at least 40% of the airfoil chord consistently with previous LES results [Christophe 2011; Christophe, Anthoine, and Moreau 2009], which leads to a delayed flow transition and re-attachment, somewhere between 40 and 65% of the chord. As such, the magnitude of flow disturbances represented by the dimensionless Reynolds stress components $\overline{u_1 u_1}/U_\infty^2$, $\overline{u_2 u_2}/U_\infty^2$, and $-\overline{u_1 u_2}/U_\infty^2$, increases substantially compared to the airfoil at 8° attack, especially close to the airfoil trailing edge.

While the time-averaged flow is found to be attached, large-scale flow distortions in form of rollers, that are reminiscent of KH-type instability, are present. These roller structures

are similar to the ones that were previously reported on the CD airfoil numerically by Christophe and Moreau [2008] at the same incidence and experimentally by Jaiswal *et al.* [2022] at a lower angle-of-attack. As the wall-normal spatial extent of these structures can be substantially larger than the mean boundary layer thickness, they have access to higher momentum flow. This explains why an increase in low-frequency convection velocity was observed despite a strong adverse pressure gradient in the trailing-edge region.

The velocity fluctuations, $-\overline{u_1 u_2}$, increases steadily before eventually getting saturated close to the trailing-edge region of the airfoil. The peak values of $-\overline{u_1 u_2}$ are shown to scale the wall-pressure spectra for two angles of attack. As such, it clearly demonstrates that the increase in the magnitude in wall-pressure statistics can be linked to an increase in $-\overline{u_1 u_2}$. The amplification of flow disturbance, such as $\overline{-u_1 u_2}$, is known to yield KH-type instability and vortex pairing in the shear layer, producing the observed roller structures [Huang and Ho 1990; Watmuff 1999; Yarusevych, Sullivan, and Kawall 2006; 2009]. In summary, these rollers are present due to the late amplification ($x > 0.4C$) of the LSB instability, and its subsequent roll-up, which ensures that large eddies reach the trailing edge of the airfoil.

Jaiswal *et al.* [2022] showed that these rollers have large coherence in the spanwise direction. Furthermore, the mode associated with roller structures correlates with the wall-pressure fluctuations at frequencies that correspond to the maximum levels of spanwise coherence. In addition, the spanwise coherence of wall-pressure and HWA spectrogram peak at the same frequency. In the absence of any alternative frequency-centred activities in the flow, it may be concluded that these rollers are responsible for an increase in the spanwise correlation length.

Finally, Lacagnina *et al.* [2019] had shown that flapping of the shear yields an increase in low-frequency noise. While the flapping of LSB may result in flapping of shear-layer, no evidence for its contribution to separation noise is found in the absence of rollers. This is because no modal structures associated exclusively with shear-layer flapping were identified. The noise mechanism due to shear-layer flapping is thus not universally present for an airfoil at near stall conditions. In the present case, the increase in flow disturbances, and the associated rolling-up of the shear layer are the only dominant flow mechanisms that contribute to separation noise.

Therefore, the question naturally arises: is the increase in the magnitude of $-\overline{u_1 u_2}$ sufficient to nullify Amiet’s diffraction theory that depends on the thin-airfoil linearized theory?

To answer this question, the radiation ratio is calculated for cases with variable flow incidence at the same Reynolds number based on chord. The results confirm that the diffraction efficacy of an airfoil subjected to higher angles of attack is substantially attenuated at frequencies associated with separation noise. This is because the overall increase in sound pressure level is comparatively small compared to the rise in spanwise correlation l_z . In particular, the energy conversion from near-field pressure to far-field pressure should be more effective as l_z increases; however, this is not achieved. Furthermore, the roller structures imply that the unsteady Kutta condition may not be valid, as its validity hinges on the flow leaving the airfoil trailing edge smoothly. As such, the diffraction efficacy for an airfoil trailing-edge that is subjected to an unsteady pressure gust due to flow separation is substantially attenuated. Nevertheless, the separation noise can be fully quantified using a compact dipole. The far-field microphones located on the either side of the airfoil confirm this dipolar behaviour along with U_∞^6 scaling of the OASPL measured in the far-field. Furthermore, the far-field acoustic pressure field directivity pattern is similar for both 8° and 15° angles of attack, which reinforces the dipolar directivity pattern. These observations partly explain why Christophe and Moreau [2008] obtained a more favourable estimate of acoustic noise while using the Ffowcs Williams and Hall [1970] analogy compared to diffraction theory [Amiet 1976] at frequencies where the separation noise dominates.

VIII. CONCLUSIONS

The present paper is a detailed aeroacoustic investigation of a CD airfoil at near stall condition. This is achieved by placing the CD airfoil at high angles of attack in an open jet anechoic wind tunnel. Two sets of experiments are performed at $Re_c \simeq 140,000$ and $Re_c \simeq 245,000$ based on airfoil chord for an airfoil placed at 15° angle of attack. For the airfoil at $Re_c \simeq 140,000$, synchronized PIV, RMP and far-field microphone measurements were performed.

The present study is driven by two fundamental research questions.

- 1) What is the mechanism that is responsible for separation noise for an airfoil near stall conditions ? If so, is it universal ?
- 2) Is the noise due to flow separation generated by a dipole for airfoil close to stall ? If so, can it be quantified by Amiet's (1976) diffraction theory ?

The present study shows that when the CD airfoil is placed at a higher angle of attack compared to 8° , such as 15° in the present study, strong amplification of flow disturbance, up to an order of magnitude higher is seen in the trailing-edge region. In fact, noise due to flow separation can be linked to increase in flow disturbances, like $-\overline{u_1 u_2}$, which scale up the wall-pressure fluctuations. This increased Reynolds stress triggers the roll up of the separated shear layer. These rollers are linked to the flow transition triggered by the Kelvin-Helmholtz instability. They are also linked to an increase in spanwise coherence of the wall-pressure fluctuations, as they convect past the trailing-edge. The modal decomposition obtained by POD shows that the modes associated with these roller structures correlate with near and far-field pressure. This correlation is observed only at frequencies where the separation noise dominates, i.e. frequency at which the $\overline{E_{11}}$ peaks. As such, rollers and associated Kelvin-Helmholtz type flow instability play a central role in the increase in noise due to flow separation. Lastly, in the present study, no contributions coming exclusively from the flapping of the shear layer were observed.

The present study conclusively shows that separation noise is dipolar in nature, therefore, quadrupole contribution for low-speed airfoils at near-stall conditions can be neglected, at least for flows up to a Mach number of about 0.1. Yet the increase in flow disturbances measured close to the trailing-edge of the airfoil implies that the assumption of small amplitude disturbance are no longer valid, which is the central premise of the thin-airfoil linearized theory used to estimate the response of the airfoil to an incoming pressure gust. Furthermore, passage of large roller structures past the trailing edge may invalidate the unsteady Kutta condition. Yet outside the frequency range at which flow separation operates, Amiet's (1976) theory should be able to predict the far-field noise even at high angles of attack as previously shown by Christophe, Anthoine, and Moreau [2009].

ACKNOWLEDGMENTS

The authors would like to acknowledge the help of Sidharth Krishnan Kalyani and Yann Pasco during the PIV measurements. Authors are thankful for computational time in supercomputer Graham, managed by the Digital research alliance of Canada.

FUNDING

This work was supported by the Canadian NSERC Discovery grant (no.RGPIN-2014-04111).

DECLARATION OF INTERESTS

The authors report no conflict of interest.

DATA AVAILABILITY STATEMENT

Raw data of PIV were processed on the Digital research alliance of Canada's HPC center. Derived data supporting the findings of this study are available from the first author upon reasonable request.

APPENDIX

In this appendix, the influence of the total length of RMP signals on wall-pressure statistics is studied, particularly at low frequencies where this parameter is known to define the lowest achievable frequency in power spectral densities.

Figure 24 first shows that this total length is an important metric when it is used to estimate the convection velocity. This in part explains as to why previous studies [Kalyani, Moreau, and Ragni 2022] have reported slightly different values of U_c and l_z . However, the uncertainty in the estimation of U_c/U_∞ is less than 10%, which yields a marginal uncertainty in the radiation ratio, Λ , when plotted on a logarithmic scale. In turn, this has no significant impact on the efficacy of diffraction theory for separation noise.

In order to understand the impact of the signal length on the spanwise correlation length (l_z), the spanwise coherence (γ^2) is plotted in figure 25 between two spanwise probes 25 and 27. The results are also compared with the data reported by Kalyani, Moreau, and Ragni [2022]. Figure 25 shows that at low-frequency oscillations, which represent uncertainty in the estimate of γ^2 , are higher for cases where the signal length is truncated below 30 seconds. Consequently, Kalyani, Moreau, and Ragni [2022], who estimated the spanwise coherence (γ^2) with a signal length of 15 seconds, have a higher uncertainty in the estimate of γ^2 .

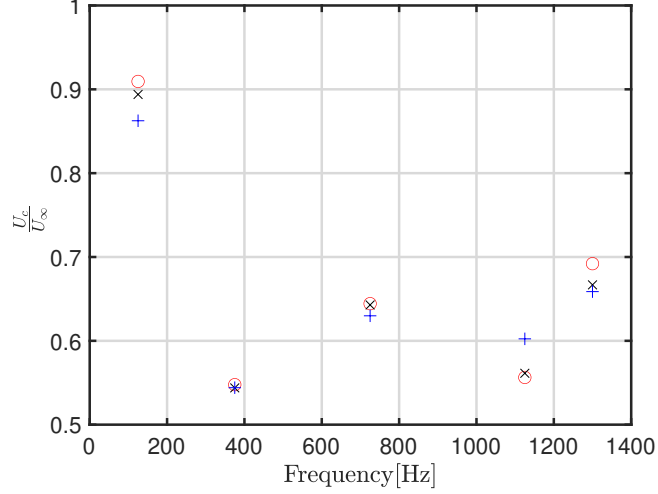


FIG. 24. Convection velocity for 15° angle of attack and $U_\infty = 16$ m/s case. Red circles corresponds to full signal length of 1 minute while blue and black crosses denote signal lengths of 20 and 30 seconds respectively.

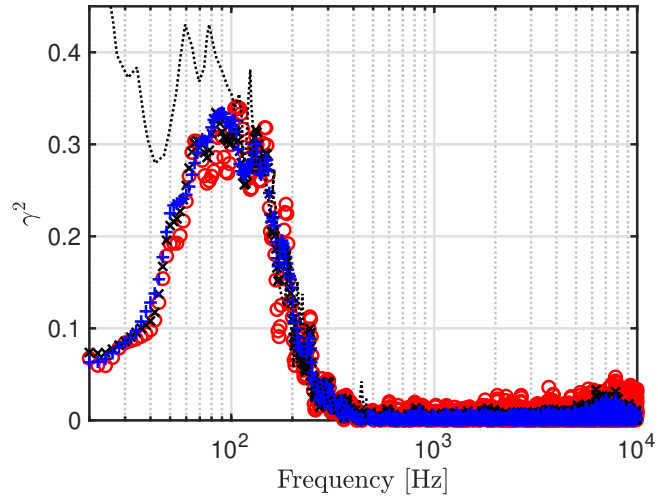


FIG. 25. Legend: γ^2 between RMP 25 and RMP 27 for 15° angle of attack and $U_\infty = 16$ m/s case. Legend for signal length same as in figure 24. Black dotted line correspond to Kalyani, Moreau, and Ragni's (2022) data.

Furthermore, Kalyani, Moreau, and Ragni [2022] took one-tenth of the number of points to estimate the PSD compared to the present case. As such, the low-frequency part of γ^2 shows an erroneous double peak in their results (see Figure 4(a) of Kalyani, Moreau, and Ragni [2022]), which is absent in the present case as well as in one reported earlier by Moreau and Roger [2005].

REFERENCES

- Abe, H., “Reynolds-number dependence of wall-pressure fluctuations in a pressure-induced turbulent separation bubble,” *Journal of Fluid Mechanics* **833**, 563–598 (2017).
- Amiet, R. K., “Noise due to turbulent flow past a trailing edge,” *Journal of sound and vibration* **47**, 387–393 (1976).
- Bertagnolio, F., Madsen, H. A., Fischer, A., and Bak, C., “A semi-empirical airfoil stall noise model based on surface pressure measurements,” *Journal of Sound and Vibration* **387**, 127–162 (2017).
- Bossomaier, T., Barnett, L., Harré, M., and Lizier, J. T., *An Introduction to Transfer Entropy: Information Flow in Complex Systems* (Springer International Publishing, 2016).
- Brooks, T. F., Pope, D. S., and Marcolini, M. A., “Airfoil self-noise and prediction,” Tech. Rep. (“NASA”, 1989).
- Caiazzo, A., Pargal, S., Wu, H., Sanjosé, M., Yuan, J., and Moreau, S., “On the effect of adverse pressure gradients on wall-pressure statistics in a controlled-diffusion aerofoil turbulent boundary layer,” *Journal of Fluid Mechanics* **960**, A17 (2023).
- Christophe, J., *Application of Hybrid Methods to High Frequency Aeroacoustics*, Ph.D. thesis, von Karman Institute for Fluid Dynamics / Universite Libre de Bruxelles (2011).
- Christophe, J., Anthoine, J., and Moreau, S., “Trailing edge noise computation of a fan blade profile,” *The Journal of the Acoustical Society of America* **123**, 3539–3539 (2008).
- Christophe, J., Anthoine, J., and Moreau, S., “Trailing edge noise of a controlled-diffusion airfoil at moderate and high angle of attack,” in *15th AIAA/CEAS Aeroacoustics Conference (30th AIAA Aeroacoustics Conference)* (Miami, Florida, 2009) p. 3196.
- Christophe, J. and Moreau, S., “LES of the trailing-edge flow and noise of a controlled-diffusion airfoil at high angle of attack,” in *Proceedings of the Summer Program* (Stanford, California, U.S.A, 2008) p. 305.
- Corcos, G., “The structure of the turbulent pressure field in boundary-layer flows,” *Journal of Fluid Mechanics* **18**, 353–378 (1964).
- Curle, N., “The influence of solid boundaries upon aerodynamic sound,” *Proceedings of the Royal Society of London. Series A. Mathematical and Physical Sciences* **231**, 505–514

(1955).

Efmitsov, B., “Characteristics of the field of turbulent wall pressure-fluctuations at large Reynolds-numbers,” *Soviet Physics Acoustics-USSR* **28**, 289–292 (1982).

Ffowcs Williams, J. E. and Hall, L. H., “Aerodynamic sound generation by turbulent flow in the vicinity of a scattering half plane,” *Journal of fluid mechanics* **40**, 657–670 (1970).

Ffowcs Williams, J. E. and Hawkings, D. L., “Sound generation by turbulence and surfaces in arbitrary motion,” *Philosophical Transactions for the Royal Society of London. Series A, Mathematical and Physical Sciences* , 321–342 (1969).

Goldstein, M. E., *Aeroacoustics* (McGraw-Hill Inc.,US, 1976).

Goody, M., “Empirical spectral model of surface pressure fluctuations,” *AIAA journal* **42**, 1788–1794 (2004).

Grasso, G., Jaiswal, P., Wu, H., Moreau, S., and Roger, M., “Analytical models of the wall-pressure spectrum under a turbulent boundary layer with adverse pressure gradient,” *Journal of Fluid Mechanics* **877**, 1007–1062 (2019).

Henning, A., Kaepernick, K., Ehrenfried, K., Koop, L., and Dillmann, A., “Investigation of aeroacoustic noise generation by simultaneous particle image velocimetry and microphone measurements,” *Experiments in fluids* **45**, 1073–1085 (2008).

Holmes, P., Lumley, J. L., Berkooz, G., and Rowley, C. W., *Turbulence, coherent structures, dynamical systems and symmetry* (Cambridge university press, 2012).

Huang, L.-S. and Ho, C.-M., “Small-scale transition in a plane mixing layer,” *Journal of Fluid Mechanics* **210**, 475–500 (1990).

Jaiswal, P., “*Etude expérimentale du bruit propre de profil aérodynamique*”, Ph.D. thesis, University of Sherbrooke, ”<http://hdl.handle.net/11143/17867>” (2020).

Jaiswal, P., Moreau, S., Avallone, F., Ragni, D., and Pröbsting, S., “On the use of two-point velocity correlation in wall-pressure models for turbulent flow past a trailing edge under adverse pressure gradient,” *Physics of Fluids* **32**, 105105 (2020).

Jaiswal, P., Pasco, Y., Yakhina, G., and Moreau, S., “Experimental investigation of aerofoil tonal noise at low mach number,” *Journal of Fluid Mechanics* **932**, A37 (2022).

Kalyani, S. K., Moreau, S., and Ragni, D., “Flow-field and noise characterization of a controlled-diffusion airfoil,” 28th AIAA/CEAS Aeroacoustics 2022 Conference. Paper number 2894. (2022).

Lacagnina, G., Chaitanya, P., Berk, T., Kim, J.-H., Joseph, P., Ganapathisubramani, B.,

Hasheminejad, S. M., Chong, T. P., Stalnov, O., Choi, K.-S., *et al.*, “Mechanisms of airfoil noise near stall conditions,” *Physical Review Fluids* **4**, 123902 (2019).

Le Floch, A., Weiss, J., Mohammed-Taifour, A., and Dufresne, L., “Measurements of pressure and velocity fluctuations in a family of turbulent separation bubbles,” *Journal of Fluid Mechanics* **902**, A13 (2020).

Ligrani, P. M. and Bradshaw, P., “Subminiature hot-wire sensors: development and use,” *J. Phys. E: Sci. Instrum.* **20**, 323–332 (1987).

Moreau, S., Christophe, J., and Roger, M., “LES of the trailing-edge flow and noise of a NACA 0012 airfoil near stall,” in *Proceedings of the Summer Program* (Stanford University, Center for Turbulence Research Stanford, CA, USA, 2008) pp. 317–329.

Moreau, S. and Roger, M., “Effect of airfoil aerodynamic loading on trailing edge noise sources,” *AIAA journal* **43**, 41–52 (2005).

Moreau, S. and Roger, M., “Back-scattering correction and further extensions of amiet’s trailing-edge noise model. part ii: Application,” *Journal of Sound and vibration* **323**, 397–425 (2009).

Moreau, S., Roger, M., and Christophe, J., “Flow features and self-noise of airfoils near stall or in stall,” 15th AIAA/CEAS Aeroacoustics Conference (30th AIAA Aeroacoustics Conference), paper number 2009-3198 (2009).

Na, Y. and Moin, P., “The structure of wall-pressure fluctuations in turbulent boundary layers with adverse pressure gradient and separation,” *Journal of Fluid Mechanics* **377**, 347–373 (1998).

Neal, D., *Effects of rotation on the flow field over a Controlled-Diffusion airfoil*, Ph.D. thesis, Michigan State University, East Lansing, MI (2010).

Pargal, S., *Non-equilibrium wall-bounded turbulence and associated noise generation*, Ph.D. thesis, University of Sherbrooke Quebec, Canada (2023).

Perennes, S. and Roger, M., “Aerodynamic noise of a two-dimensional wing with high-lift devices,” in *4th AIAA/CEAS aeroacoustics conference* (Toulouse, France, 1998) p. 2338.

Raus, D., Cotté, B., Monchaux, R., Jondeau, E., Souchotte, S., and Roger, M., “Experimental study of the dynamic stall noise on an oscillating airfoil,” *Journal of Sound and Vibration* **537**, 117144 (2022).

Roger, M. and Moreau, S., “Broadband self noise from loaded fan blades,” *AIAA journal* **42**, 536–544 (2004).

Roger, M. and Moreau, S., “Back-scattering correction and further extensions of Amiet’s trailing-edge noise model. Part 1: theory,” *Journal of Sound and vibration* **286**, 477–506 (2005).

Roger, M. and Moreau, S., “Addendum to the back-scattering correction of Amiet’s trailing-edge noise model,” *Journal of Sound and vibration* **331**, 5383–5385 (2012).

Sanjose, M., Towne, A., Jaiswal, P., Moreau, S., Lele, S., and Mann, A., “Modal analysis of the laminar boundary layer instability and tonal noise of an airfoil at Reynolds number 150,000,” *International Journal of Aeroacoustics* **18**, 317–350 (2019).

Schloemer, H. H., “Effects of pressure gradients on turbulent-boundary-layer wall-pressure fluctuations,” *The journal of the acoustical society of America* **42**, 93–113 (1967).

Sirovich, L., “Turbulence and the dynamics of coherent structures. i. coherent structures,” *Quarterly of applied mathematics* **45**, 561–571 (1987).

Spalart, P. R., Belyaev, K. V., Shur, M. L., Kh Strelets, M., and Travin, A. K., “On the differences in noise predictions based on solid and permeable surface flows williams–hawkins integral solutions,” *International Journal of Aeroacoustics* **18**, 621–646 (2019).

Turner, J. M. and Kim, J. W., “Quadrupole noise generated from a low-speed aerofoil in near-and full-stall conditions,” *Journal of Fluid Mechanics* **936**, A34 (2022).

Venkatraman, K., Moreau, S., Christophe, J., and Schram, C., “Numerical investigation of h-darrieus wind turbine aerodynamics at different tip speed ratios,” *International Journal of Numerical Methods for Heat & Fluid Flow* (2023).

Watmuff, J. H., “Evolution of a wave packet into vortex loops in a laminar separation bubble,” *Journal of Fluid Mechanics* **397**, 119–169 (1999).

Wu, H., Laffay, P., Idier, A., Jaiswal, P., Sanjosé, M., and Moreau, S., “Numerical study of the installed controlled diffusion airfoil at transitional Reynolds number,” in *Mathematical and Computational Approaches in Advancing Modern Science and Engineering* (Springer, 2016) pp. 505–515.

Wu, H., Moreau, S., and Sandberg, R., “Effects of pressure gradient on the evolution of velocity-gradient tensor invariant dynamics on a controlled-diffusion aerofoil at $Re_c = 150000$,” *Journal of Fluid Mechanics* **868**, 584–610 (2019).

Wu, H., Moreau, S., and Sandberg, R. D., “On the noise generated by a controlled-diffusion aerofoil at $Re_c = 1.5 \times 10^5$,” *Journal of Sound and Vibration* **487**, 115620 (2020).

Yarusevych, S., Sullivan, P. E., and Kawall, J. G., “Coherent structures in an airfoil bound-

ary layer and wake at low Reynolds numbers,” *Physics of Fluids* **18**, 044101 (2006).

Yarusevych, S., Sullivan, P. E., and Kawall, J. G., “On vortex shedding from an airfoil in low-Reynolds-number flows,” *Journal of Fluid Mechanics* **632**, 245–271 (2009).

Zang, B., Mayer, Y. D., and Azarpeyvand, M., “Experimental investigation of near-field aeroacoustic characteristics of a pre-and post-stall naca 65-410 airfoil,” *Journal of Aerospace Engineering* **34**, 04021080 (2021).